Faults in conventional flow simulation models: a consideration of representational assumptions and geological uncertainties

T. Manzocchi[1], A. E. Heath[2], B. Palananthakumar[1], C. Childs[1] and J. J. Walsh[1]
[1]*Fault Analysis Group, UCD School of Geological Sciences, University College Dublin, Dublin 4, Ireland (e-mail: tom@fag.ucd.ie)*
[2]*Fault Analysis Group, Department of Earth and Ocean Science, University of Liverpool, Liverpool L69 3GP, UK*

ABSTRACT: Even when geologically based methods are used to determine fault rock permeabilities and thicknesses for input into flow simulators, a wide range of simplifying assumptions regarding fault structure and content are still present. Many of these assumptions are addressed by defining quantitative and flexible methods for realistic parameterization of fault-related uncertainties, and by defining automated methods for including these effects routinely in full-field flow simulation modelling. The fault effects considered include: the two-phase properties of fault rocks; the spatial distributions of naturally variable or uncertain single-phase fault rock properties and fault throws; and the frequencies and properties of sub-resolution fault system or fault zone complexities, including sub-seismic faults, normal drag and damage zones, paired slip surfaces and fault relay zones. Innovative two-phase or geometrical upscaling approaches implemented in a reservoir simulator pre-processor provide transmissibility solutions incorporating the effect, but represented within the geometrical framework of the full-field flow simulation model. The solutions and flexible workflows are applied and discussed within the context of a sensitivity study carried out on two faulted versions of the same full-field flow simulation model. Significant influence of some of these generally neglected fault-related assumptions and uncertainties is revealed.

KEYWORDS: *fault permeability, fault transmissibility, uncertainty, variability, oil production, fault rock, fault zone, fault throw, relay zones, two-phase flow*

INTRODUCTION

Over recent years it has become increasingly routine to apply geologically based methods for calculating fault transmissibility multipliers in full-field flow simulation studies of clastic reservoirs (e.g. Knai & Knipe 1998; Ottesen Ellesevet *et al.* 1998; Manzocchi *et al.* 1999; Childs *et al.* 2002, Hollund *et al.* 2002; Rivenæs & Dart 2002; Yielding 2002; Jolley *et al.* 2007; Myers *et al.* 2007). These methods calculate multipliers for each fault connection in the model based on local estimates of fault rock permeability and thickness. Fault permeability is generally determined from empirical correlations against fault rock shale content, with the latter estimated from a fault surface clay content proxy-property (often the Shale Gouge Ratio; Yielding *et al.* 1997) for faults formed at different burial depths (e.g. Manzocchi *et al.* 1999; Fisher & Knipe 2001; Crawford *et al.* 2002; Sperrevik *et al.* 2002). Fault rock thickness is estimated from correlations against fault throw, perhaps also including a secondary term governing lithological dependence (e.g. Hull 1988; Beach *et al.* 1999; Childs *et al.* 2007). These properties are then combined with the permeability and geometry of the juxtaposed cells to give a multiplier for each faulted connection (see Manzocchi *et al.* 1999, for details).

Although this relatively new workflow is a significant advance on previous *ad hoc* treatments of fault transmissibility multipliers since it ensures that the faults are plausible geologically, a host of simplifying assumptions are still present (e.g. Hesthammer & Fossen 2000). The omission from the workflow of two-phase fault rock effects has received considerable recent attention (e.g. Manzocchi *et al.* 1998, 2002; Fisher *et al.* 2001; Rivenæs & Dart 2002; Al-Busafi *et al.* 2005), but other complications are known to occur naturally on faults but are generally omitted from simulation models despite recognition that they may have an influence. These include localized normal drag or damage zones (e.g. Hesthammer & Fossen 2000; Hesthammer *et al.* 2000; Shipton & Cowie 2001, 2003; Odling *et al.* 2004), displacement partitioning onto paired slip surfaces (e.g. Childs *et al.* 1997; Foxford *et al.* 1998) and the presence of discrete fault relay zones (e.g. Dawers & Anders 1995; Huggins *et al.* 1995; Childs *et al.* 1995).

In addition, natural faults are extremely variable in terms of thickness, content and structure over small distances (e.g. Childs *et al.* 1996; Foxford *et al.* 1998, Bonson *et al.* 2007), and core analysis indicates that fault rock derived from the same rocks under the same conditions can have permeabilities varying over a couple of orders of magnitude (e.g. Gibson 1998; Fisher & Knipe 1998, 2001; Sperrevik *et al.* 2002; Jolley *et al.* 2007). A correct representation of this heterogeneity depends on the correlation length of the variability. Manzocchi *et al.* (1999) assumed that the correlation length of the variability is considerably smaller than the size of a simulation grid-block

and, given this assumption, showed that the harmonic average fault rock thickness and arithmetic average fault rock permeability from the assumed property distributions are appropriate for inclusion in the multiplier calculation. There are, however, few field data on fault property correlation lengths, which may therefore be considerably larger than the size of a simulator grid-block. In this case, the expected variability should, perhaps, be modelled stochastically and represented explicitly in the simulation model (e.g. Flodin *et al.* 2001).

A further geological uncertainty generally not included in simulation modelling sensitivity studies concerns fault juxtapositions. A correct representation of fault juxtaposition is generally considered to be the single most important fault-related issue in most reservoir simulation studies, yet fault throws can seldom be mapped with complete confidence. Interpretations can be ambiguous, and the uncertainty of fault throw depends also on the quality of the seismic data. Since natural faults also show variability in fault throw along their length at a higher frequency than the throw variations that might be mapped in a subsurface reservoir (e.g. Muraoka & Kamata 1983; Manighetti *et al.* 2001), it is likely that in many instances insufficient throw variability is included in the simulation model, exacerbating the overall uncertainty in fault throw. Like the variability in fault rock properties, therefore, sensitivity to variability in fault throw arising both from natural, but seismically irresolvable, high frequency fluctuations should be considered, as well as from possible lower-frequency misinterpretations. Another uncertainty derives from the well-known issue that faults interpreted from seismic data often have artificially high throw gradients at their tips, owing to these portions of the fault being below seismic resolution (e.g. Watterson *et al.* 1996; Yielding *et al.* 1996). In addition, a more extreme manifestation of throw uncertainty is the suspected presence of sub-seismic faults (e.g. Gauthier & Lake 1993; Walsh *et al.* 1998), which are seldom included in anything other than the simplest fashion in full-field simulation models.

The objectives of this paper are to discuss solutions to some of these petrophysical and geometrical fault-related simplifications and uncertainties, and to assess in an example reservoir what their implications on field-wide oil production might be. An important aspect of the work is finding plausible quantitative expressions to describe the features of interest (e.g. the locations of relay zones of particular sizes on otherwise continuous faults, or the fraction of fault throw accommodated by a damage zone). A feature may be so complex or naturally variable that it has been described only in qualitative terms in the geological literature. However, if these features are to be modelled systematically in an automated manner, equations describing their frequency and/or geometry and/or petrophysical properties must be supplied. A familiar example of such an expression is the recognition some 15 years ago that the frequency of sub-seismic faults of particular sizes might be predicted through extrapolation of the power-law population of seismically resolvable faults (e.g. Childs *et al.* 1990; Heffer & Bevin 1990; Westaway 1994). This paper presents flexible expressions for defining stochastic populations of fault relay zones, for defining the amount of fault throw accommodated by ductile drag (or minor brittle faulting if a damage zone is present) around faults of different sizes, and for defining relevant two-phase fault rock properties from their absolute permeability. Although they are plausible geologically, these expressions are not the most accurate possible and their general application is not necessarily advocated. In a similar way that Manzocchi *et al.* (1999) presented an equation linking Shale Gouge Ratio (SGR) and fault throw to fault permeability based on scant public domain data, but advised that case-specific information (ideally inverted from reservoir flow information) should be used instead if possible, these new expressions are often little more than first estimates for an engineering application. A numerical tool needs a quantitative input expression, and the equations should be considered within this context.

A second crucial aspect of the work is identifying a means of representing the feature of interest in the simulator without compromising unduly either the performance of the simulator or the geometrical/petrophysical characteristics of that feature. Manzocchi *et al.* (2002), for example, showed that two-phase fault rock properties can be included through the use of directional, irreversible pseudorelative permeability curves by upscaling the effects of the two-phase fault rock properties into the adjacent grid-blocks. This workflow (with a few modifications) has been implemented in the reservoir simulator preprocessor applied in the present work. The workflow is not, however, necessarily the optimum way of modelling two-phase fault rock properties, and explicit fault rock grid-blocks with extreme local grid refinements in and around faults should, in principle, provide a more accurate solution (e.g. Manzocchi *et al.* 1998; Rivenæs & Dart 2002). This, however, is impractical in full-field simulation modelling, since the tools needed for making and populating the locally refined grids are in their infancy, and because these grids would reduce the speed of the simulator tremendously. Therefore, a modified version of the compromise workflow proposed by Manzocchi *et al.* (2002) is used.

The compromise devised for representing the geometrical aspects of the faults is through a process referred to as 'geometrical upscaling'. This involves the definition of transmissibilities for connections that do not necessarily exist in the simulation model, and modifications to those that do. For example, if the throw on a fault at a particular location in a simulation model is eight times larger than the thickness of the cells, but this throw is halved in a particular realization of the reservoir structure because of local stochastic throw uncertainty, then the transmissibilities of the connections that exist explicitly in the model are set to zero (since these juxtapositions do not exist in the realization), and new, implicit, non-neighbour connections defining the juxtapositions present in the realization are added to the simulation input deck, with transmissibilities representative of the thickness and permeability of the revised (lower throw) fault. This method, which is described in detail later, can be used to represent both modifications of the throws of faults on planar fault surfaces (as discussed above), as well as the more complex, three-dimensional flow paths arising from multiple slip surfaces or relay zones. Since these features, although 3D, occupy only the volume of grid-block close to its faulted edge, modelling their effects in this manner (rather than by modifying the grid geometry) ensures that volumetric artefacts are not introduced. An additional, but significant, boon of using this method is that although each realization of the reservoir structure might contain a vastly different reservoir geometry in terms of fault throws and cell juxtapositions, only a few input files listing connection transmissibilities need to be changed in the simulation model input deck to reflect the different structural realization: the overall geometry of the simulation model is unaltered.

These new methods are illustrated and discussed within the context of a sensitivity study on a synthetic reservoir model. The model and the simulation results are summarized in the following section. Discussions of the different structural realizations used and a consideration of how these have influenced production are then presented under the three, loose topics of fault rock effects (including stochastic variations in fault permeability and deterministic inclusion of two-phase fault rock

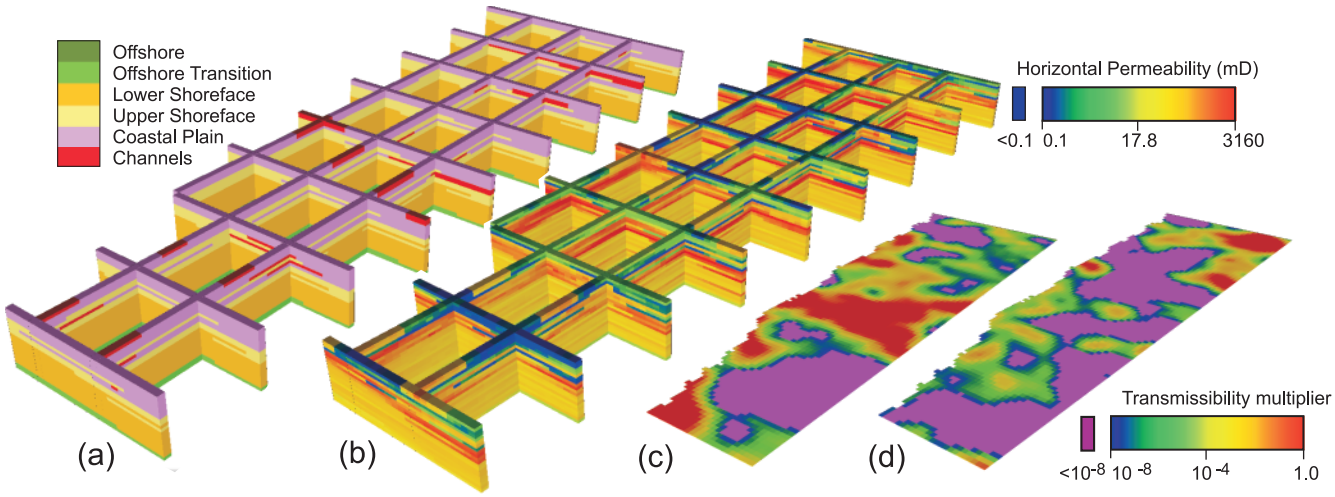

Fig. 1. Sedimentological characteristics of the simulation model: (**a**) facies associations; (**b**) horizontal permeability; (**c**, **d**) transmissibility multipliers between layers 5 and 6 (c) and 10 and 11 (d) reflecting variably cemented parasequence boundaries. The model area is 9 km by 3 km and is 80 m thick. The model is number 106 shown in Figure 6 of Manzocchi *et al.* 2008*a*.

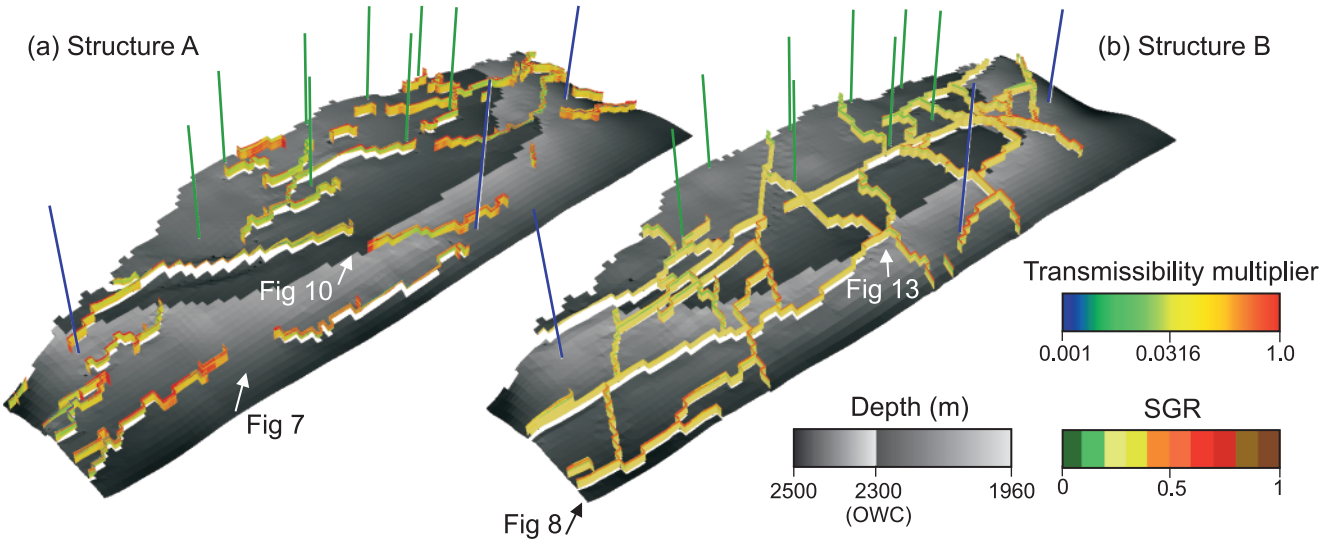

Fig. 2. Overview of the two datum faulted models. The bottom layers are shown coloured by depth. Fault connections are coloured (**a**) by the datum transmissibility multiplier in Structure A and (**b**) by the Shale Gouge Ratio in Structure B. Production wells are green, injection wells are blue. Arrows indicate the approximate viewpoints for the indicated figures.

properties), fault throw effects (including throw uncertainty and sub-seismic faults) and fault zone effects (including normal drag and damage zones, paired slip surfaces and stochastic populations of fault relay zones).

MODELS AND RESULTS

The effects on oil production of the various fault-related representations are assessed on two structural versions of the same synthetic reservoir model taken from a large modelling programme which is described elsewhere (see Manzocchi *et al.* 2008*a* for a synopsis). The 9 km × 3 km model is of a wave-dominated shoreface orientated parallel to the long axis of the reservoir and comprises four, 20 m thick parasequences (Fig. 1). The sedimentology is modelled with a low aggradation angle and hence the overall stratigraphy is approximately layer-cake (Fig. 1a). The uppermost parasequence contains poor quality coastal plain facies (horizontal permeability (k_H) of *c.* 3 mD; zero vertical permeability (k_V)), with a few good quality (k_H≈450 mD, k_V≈90 mD) distributory channels, overlying high permeability (k_H≈850 mD, k_V≈160 mD) upper shoreface facies. Lower parasequences are more distal, and gradually pass into lower shoreface (k_H≈90 mD, k_V≈1.65 mD) and transitional (k_H≈20 mD, k_V =0) facies, resulting in a downward decrease in both reservoir quality and heterogeneity (Fig. 1b). Each parasequence-bounding surface is cemented over 90% of its area, with the cements represented as vertical transmissibility multipliers (Figs 1c, d). The two structural versions considered are of a non-compartmentalized system of faults orientated predominantly perpendicular to the waterflood direction (Structure A, Fig. 2a), and a more isotropic, compartmentalizing system of faults (Structure B, Fig. 2b). The largest faults in each case have maximum throws slightly less than the reservoir thickness (i.e. 80 m). The reservoir model contains fluids based on those in the UK Brent Province, and is developed through a voidage replacement waterflood, using eight production and three injection wells. The former are located at the crest or close to the mid-point of the flank of the structure; the latter located in the water-leg

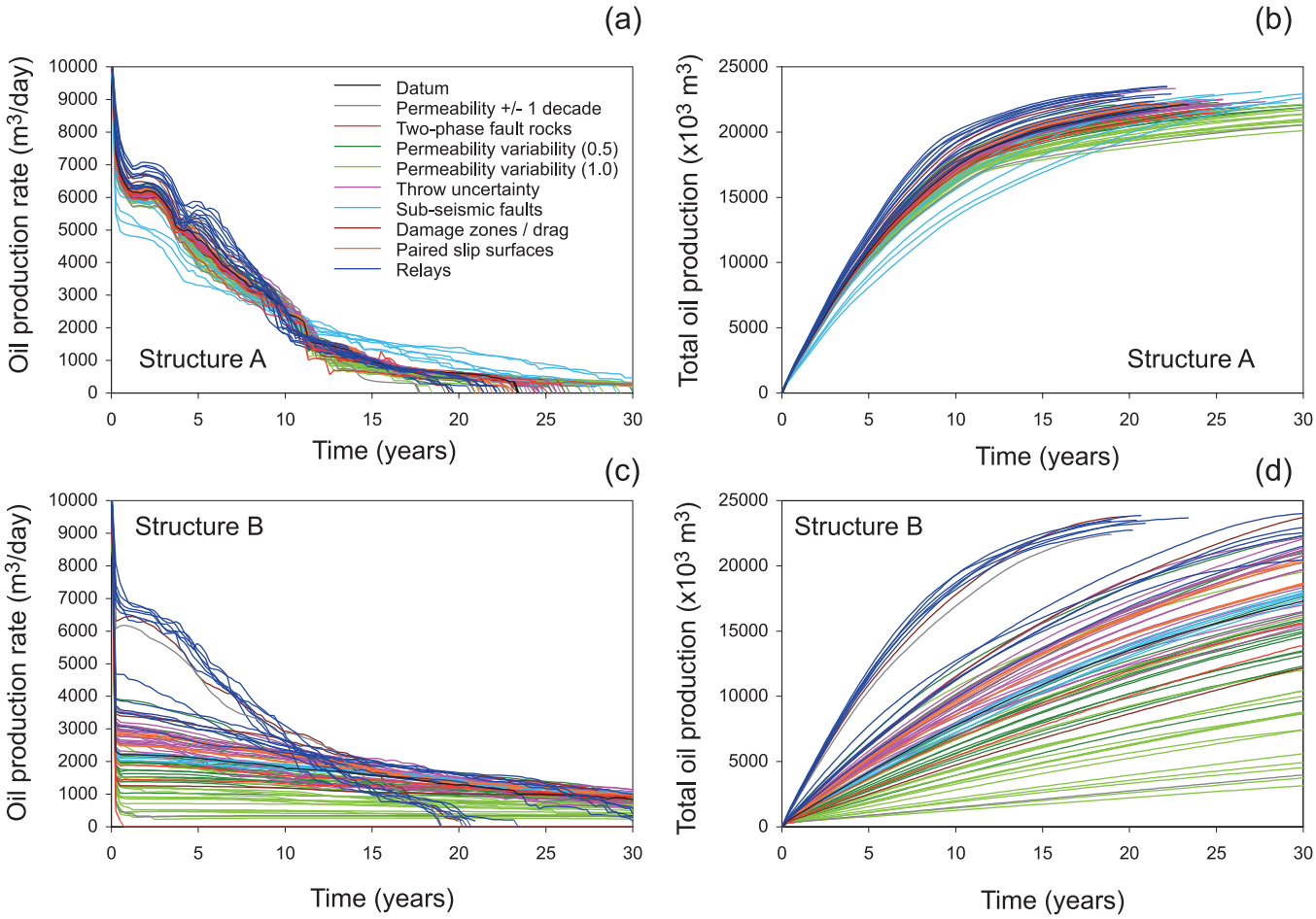

Fig. 3. Oil production rates and total oil production profiles for (**a**, **b**) Structure A and (**c**, **d**) Structure B reservoirs. The curves are coloured by the effects indicated on the legend in (a). The numbers in parentheses for the permeability variability cases refer to the standard deviations of the two distributions used.

(Fig. 2). These wells are positioned without reference to the faults; hence the development is not conditioned to either fault system. Production is simulated for up to 30 years, subject to minimum well-specific and field-wide oil production rate cut-offs. Further details of sedimentological, structural and reservoir engineering aspects of the models are given by Howell *et al.* (2008), Manzocchi *et al.* (2008*b*), Matthews *et al.* (2008) and Stephen *et al.* (2008).

Fault rock thickness (t_f) is determined throughout from fault throw (d_f) using the expression $t_f = d_f/170$ (Manzocchi *et al.* 1999). Fault rock permeability (k_f) is determined as a function of SGR (Yielding 2002) using the relationship $k_f = 10^{-1.6-4\mathrm{SGR}}$. As shown later (Fig. 9), this is broadly representative of laboratory measurements of phyllosilicate framework fault rocks from North Sea Brent Province reservoirs (Jolley *et al.* 2007). The transition from juxtaposition-dominated production behaviour to fault rock-dominated behaviour in the suite of models from which this one derives occurs over a permeability range of approximately two orders of magnitude, and the datum permeability model used in this study is situated close to the centre of this range (Manzocchi *et al.* 2008*b*). Hence, for more permissive permeability models, the behaviour of the two structures (A and B) is fairly similar. In less permissive ones the compartmentalization of Structure B is of paramount importance, and the performance of Structure B reservoirs is much worse than Structure A reservoirs, within which tortuous flow paths from injectors to producer exist around the faults (Manzocchi *et al.* 2008*b*). Therefore, one can expect that oil production in the reservoirs will show more sensitivity to details of the fault systems given the datum fault permeability model used in this study than they would, for example, if a more permissive reference property model were used (the datum case used in this study was selected precisely for this reason).

Results considered in this study derive from 84 simulation models for each of the two structures, and each model includes a single fault-related factor generally omitted from simulation studies (Figs 3, 4). That combinations of these factors have not been considered within a single model has the advantage that the effect of the specific factor can be isolated, but has the disadvantage that the suite of models are not capturing the full extent of likely variability in production response. Since the objectives of this study are to describe methods for including these factors and to discuss their effects, the approach taken is appropriate. Some factors are modelled entirely deterministically (e.g. the two-phase fault rock properties or the damage zones) and, for these, different models have been simulated based on different geological input assumptions. Other factors also include a stochastic component (e.g. the permeability variability and throw uncertainty). The results for these are shown for different model realizations (usually six, but sometimes three) derived from different geological assumptions. The simulation input for each case was prepared in TransGen, the authors' fault property simulator pre-processor, and the flow simulations were run in Eclipse.

As well as by comparison with the datum case, which contains the same permeability predictor but in which all

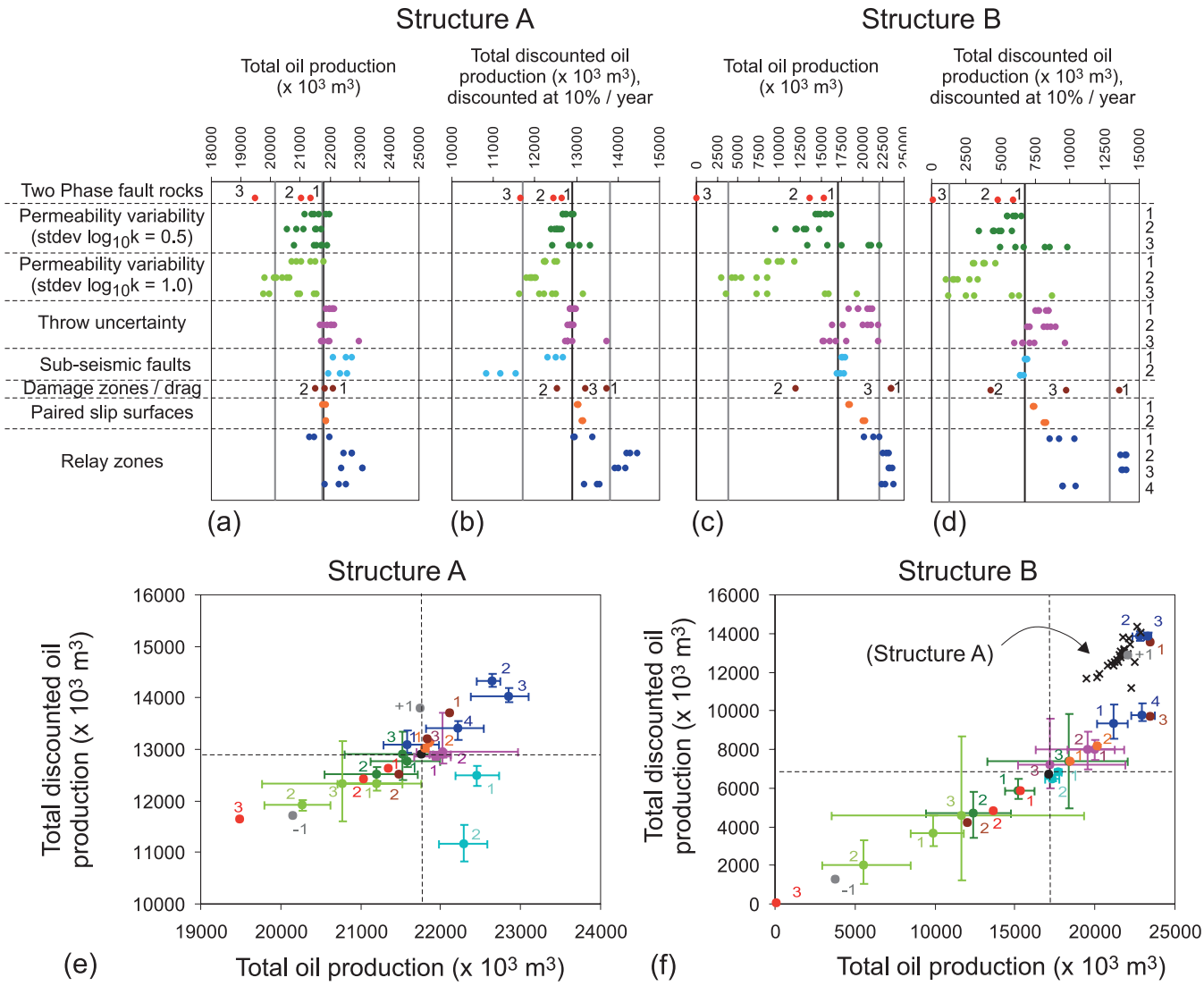

Fig. 4. Total oil production after 30 years and total discounted oil production for the (**a**, **b**) Structure A and (**c**, **d**) Structure B reservoirs. Note that different scales are used on each graph. Colours correspond to those used in Figure 3, and the numbers (1, 2, 3, 4) refer to the different parameterizations of similar effects discussed in the text. The vertical lines show the datum case in black and the other two reference cases in grey. The two-phase fault rock property and damage zone/drag cases are different deterministic cases, while results are shown for three or six realizations of the stochastic cases. (**e**, **f**) Cross-plots of total oil production against discounted oil production for the two structures, using the same colour scheme. The error bars span the total range obtained in all realizations of each case (numbered as in a–d). The dashed lines show the datum case, and the black crosses in (f) reproduce the averages for Structure A.

additional factors are omitted, it is useful to compare the results with models in which fault permeabilities are one order of magnitude more and less permissive than the datum case. Recovery factors for the Structure A versions of these reference models are 41.6% when the more permissive case is used, 41.9% using the datum case and 40.4% using the less permissive case (the higher recovery factor for a lower permeability case is because of increased sweep efficiency, and is discussed in detail by Manzocchi *et al.* 2008*b*). The same three cases have recovery factors of 42%, 37.5% and 9.8% when the reservoir contains the Structure B fault system.

Field-wide oil production curves for all models are shown in Figure 3, colour-coded by the factor considered. Figure 4 summarizes the results with respect to total oil production and to total discounted oil production calculated using a discount factor of 10% per year. A few general observations can be made from Figure 4 before individual cases are discussed in the following sections. Inclusion of some features can have a significantly larger effect on production than changing the deterministic fault rock permeability model by an order of magnitude. The different cases have more of an impact in absolute terms on the compartmentalized Structure B reservoir, but when compared with the range spanned by the more and less permissive reference cases, the total ranges are similar. The effects of the factors can be both detrimental or beneficial, and different factors can have different effects, depending on whether the discounted or non-discounted production is considered for a particular structure, as well as depending on the structure itself (Figs 4e, f).

FAULT ROCK EFFECTS

It has been suggested on theoretical grounds that two-phase fault rock properties should have an increasingly significant role in production from faulted reservoirs as capillary forces become relatively more significant (e.g. Ringrose *et al.* 1993; Ringrose & Corbett 1994; Manzocchi *et al.* 1998, 2002; Fisher & Knipe 2001). To date, however, effects of two-phase fault rock

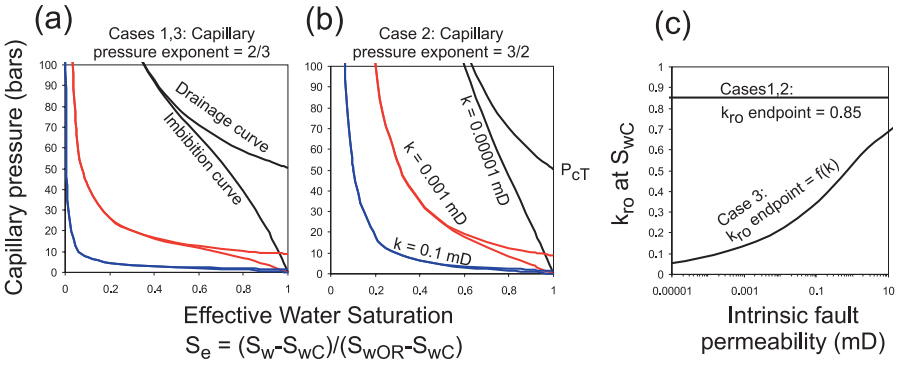

Fig. 5. Input two-phase property cases. (**a**, **b**) Capillary pressure curves for three different fault rock permeabilities (indicated by colour and labelled in b) used in (a) Cases 1 and 3 and (b) Case 2. The upper curve in each case is the drainage one and the lower curve the imbibition one. (**c**) Permeability-dependent oil relative permeability endpoint used in Case 3, compared to the constant endpoint used in Cases 1 and 2. See text and Appendix A for details.

properties have been investigated only in more-or-less contrived small-scale models (e.g. Ringrose *et al.* 1993; Manzocchi *et al.* 1998, 2002; Rivenæs & Dart 2002; Al-Busafi *et al.* 2005; Berg & Øian 2007). The example reservoirs used in this study – although synthetic – contain scales, rates, fluids and pressures representative of real reservoirs (Manzocchi *et al.* 2008*a*, Matthews *et al.* 2008) and are, therefore, a good test of whether two-phase fault rock properties may, indeed, be of practical significance. The workflow used to allow routine inclusion of two-phase fault rock properties in the simulation models is described below, and the results for three different input assumptions discussed.

The second set of fault rock effects investigated relate to spatial variability in single-phase permeability. Permeability is assumed to follow the datum k_f/SGR relationship, but, at any particular SGR, to be distributed log-normally according to different variability magnitudes. These distributions are modelled stochastically over the fault surfaces using different models for the correlation lengths of the variability. The results show sensitivity to both the correlation length and magnitude of the variation.

Effects of two-phase fault rock properties

Effects of two-phase fault rock properties are included using a generalized and streamlined version of the workflow proposed by Manzocchi *et al.* (2002). In this workflow, expressions defining two-phase fault rock properties (saturation-dependent relative permeability and capillary pressure curves for faults in either the drainage or imbibition cycles) are defined as input. In the present study, the relationships proposed by Manzocchi *et al.* (2002) define the datum set of two-phase properties referred to as Case 1 (Fig. 5). In Case 2 the capillary pressure curves are modified to reflect more poorly-sorted fault rocks (Fig. 5b) and, in Case 3, the fault rock oil relative permeability curves are made dependent on the intrinsic fault rock permeability (Fig. 5c). Further details of the equations used in the three cases are given in Appendix A.

The two-phase fault rock properties are used in conjunction with static model properties, and across-fault flow rates read from simulator restart files to derive upscaled pseudorelative permeability functions for cell faces adjacent to faults (Table 1). The upscaling (or pseudoization) is performed using the analytical solution, based on work by Marle (1981) and Dale *et al.* (1997), shown schematically in Figure 6. The volume of interest comprises a reservoir grid-block and a narrow volume of lower permeability fault rock at the downstream edge of the block. The objective of the pseudoization is to determine the upscaled relative permeability functions of the system for the particular oil and water properties and flow rate present.

Consider the red curve in Figure 6a. Assume that the water saturation at the downstream edge of the fault rock is known (S_{w1} in Fig. 6a) and that a particular fractional flow (f_W ; the fraction of the total flow occupied by the water phase) is active. A system of governing equations then defines the saturation profile in the fault rock as a function of the oil and water viscosities, total flow velocity, and single- and two- phase fault rock properties present (Dale *et al.* 1997). This results in water saturation S_{w2} in the fault rock at the interface with the grid-cell (Fig. 6a). By assuming capillary pressure equivalence (at a value of P_{C2}) between the fault rock and the reservoir rock across

Table 1. *Derivation of the parameters needed to include the two-phase fault rock properties in the simulation models*

Parameter	Derivation
The flow rate (Darcy velocity) across the faulted connection.	Derived from information contained in the static model and in the simulator restart files.
The permeability, porosity and length of the upstream grid-block.	Contained in the static simulation model. The upstream grid-blocks are identified from the flow rate information. Zero-flow rate directional pseudos are calculated and assigned to the relevant faces of downstream grid-blocks.
The relative permeability and capillary pressure functions of the upstream grid-block.	Contained in the simulation model input deck.
The permeability, porosity and thickness of the fault rock.	Calculated according to user-defined relationships (in these models as functions of throw and SGR).
The relative permeability and capillary pressure functions of the fault rock.	Calculated as a function of the single-phase fault properties according to user-defined relationships.
The hydrocarbon-water contact and fluid viscosities and densities at reservoir conditions.	Contained in the simulation model input deck.
The upscaling method used.	Depends on whether the fault connection is in the drainage or imbibition cycle. This is determined from the original hydrocarbon–water contact, the oil and water densities and the local capillary threshold pressure of the fault rock. The last of these is determined from the drainage fault rock capillary pressure function at an effective water saturation of 1.0.

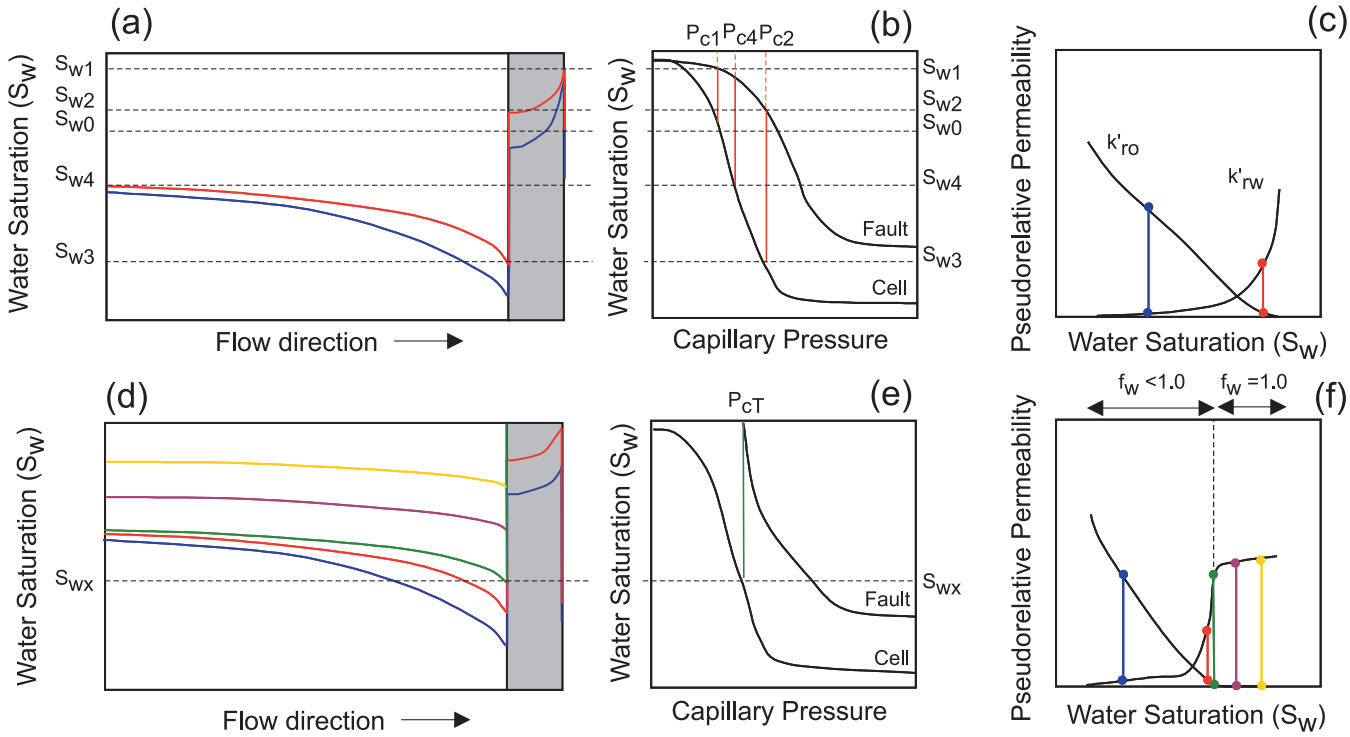

Fig. 6. Schematic cartoon of the analytical upscaling method used for fault faces in (**a–c**) the imbibition cycle and (**d–f**) the drainage cycle. The cell is shown in white and the fault rock in grey (a, d). The saturations and capillary pressures labelled in (a) and (b) refer to points on the red saturation profile shown in (a) and are discussed in the text. The red and blue vertical lines in (b) represent the capillary equilibrium points across fault rock to reservoir rock interfaces related to the red curve in (a). The coloured points in (c) and (f) are oil and water pseudorelative permeabilities derived from the saturation profiles shown in equivalent colours in (a) and (d). See text for discussion.

this interface, the water saturation at the downstream edge of the grid-block (S_{w3}) can be established (Fig. 6b). Once this is known, the saturation profile in the grid-block can then be derived as far as the inlet of the cell (S_{w4}; Fig. 6a). Hence, the saturation profile in both media can be established for this fractional flow, provided that the saturation at the downstream edge of the fault rock (S_{w1}) is known. Dale *et al.* (1997) were concerned with steady state flow in periodically heterogeneous media and, therefore, they converged on a value of S_{w1} such that the capillary pressure at the inlet (i.e. P_{C4}, related to S_{w4} in the cell) is equal to the capillary pressure at the outlet (P_{C1}, related to S_{w1} in the fault rock). Since the geometrical boundary conditions relevant to the problem here are different, it is assumed that the capillary pressure at the outlet (P_{C1}) is equal to the capillary pressure at the asymptotic saturation of the grid-block (S_{w0}). S_{w0} is equal to the water saturation that would be present immediately downstream of the fault if the reservoir rock here has identical properties to the reservoir rock on the upstream side of the fault for the flow velocity and fractional flow present, and if the two-phase effects of any faults downstream of the fault in question do not influence this interface. These factors are an obvious simplification of the reservoir conditions; however, they are a reasonable engineering compromise maintaining a relatively simple workflow involving only one grid-block.

Once the saturation profile has been established, the oil and water phase permeabilities at any point in the volume of interest are determined from the input functions for the cell and fault rock, and a harmonic average then yields the effective phase permeabilities. These are converted to pseudorelative permeabilities by normalizing against the effective intrinsic permeability and are indexed to the pore volume-weighted average saturation of the volume of interest. This results in the definition of one point on the oil and water pseudorelative permeability curve (Fig. 6c). Repeating the process for fractional flows in the range $10^{-12} \leq f_W \leq 1-10^{-12}$ defines the pseudorelative oil and water permeability functions for $S_{wC} < S_w < S_{wOR}$. Determination of the endpoint saturations and pseudorelative permeabilities requires special treatments not discussed here (see Badley Geoscience 2004 for details).

The procedure described above is appropriate if the fault rock capillary pressure is zero when the effective water saturation is 1.0; i.e. if the fault is in the imbibition cycle. The procedure is slightly more complex if the fault rock is in the drainage cycle since, in this case, the capillary pressure in the fault must exceed the capillary threshold pressure of the fault rock (P_{CT} in Fig. 6e) for the fault to be permeable to oil. The same procedure as in the imbibition cycle is used for profiles in which the capillary pressure at the interface between the reservoir rock and the fault rock is greater than the capillary threshold pressure of the fault rock (S_{wx} in Fig. 6d). These profiles (blue and red curves in Fig. 6d) all have $f_W < 1$, and result in $k'_{ro} > 0$ (Fig. 6f). A number of further curves (green, purple, yellow in Fig. 6d) are generated by varying the capillary pressure at the interface between the reservoir rock and fault rock in the range $P_{cT} \geq P_C \geq 1$ Pa for a constant fractional flow of 1.0. This defines the portion of the pseudorelative permeability curve for k'_{rw} over which $k'_{ro} = 0$ (Fig. 6f).

The upscaled solutions, which have been checked extensively against those obtained numerically (e.g. Manzocchi *et al.* 2002), depend on eight local parameters. The first four are the permeability, thickness, length (perpendicular to the faulted face) and two-phase property functions of the upstream grid-block (six different facies associations are present in the models, each of which is assigned a different set of cell-scale relative permeability functions). The final four are the permeability and thickness of the fault rock, the across-fault flow rate and whether the fault connection is in the imbibition or drainage

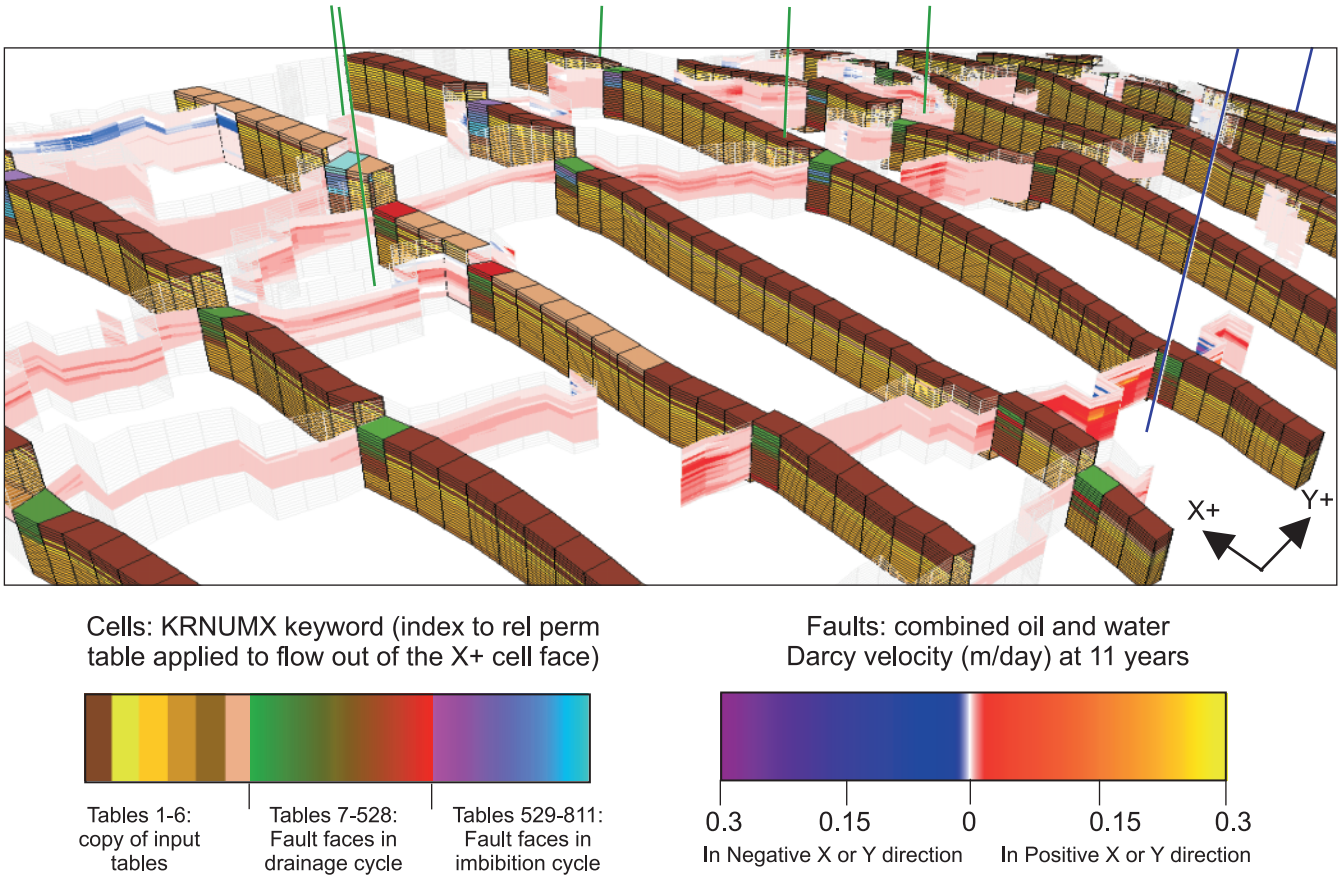

Fig. 7. Example of the two-phase workflow updated for the fourth time (11 years into the field life) for Case 2 in Reservoir A. Faults are coloured by Darcy velocity, and cells by index to the irreversible directional relative permeability tables determined for flow out of cells in the X+ direction. Where the face of this cell is unfaulted (or is not connected to any active cells) the input tables (1–6) are used, but new tables (7–811) are assigned when the face is faulted. Three other sets of indices control flow in the X−, Y+ and Y− directions, while the input tables control flow in the Z and Z− directions. See text for discussion.

cycle. Note that there is no separate dependence on the two-phase fault rock properties since, in the procedure used, these depend exclusively on the intrinsic fault permeability (see Appendix A). As it is impractical to calculate a unique solution for each of the 10 000+ fault connections in a faulted simulation model, groupings of connections sharing identical (for the discrete variables) or similar (for the continuously varying properties) parameters are identified. Additionally, since across-fault flow rates can vary over the course of a model run, greater accuracy can be achieved if the pre-processor and the simulator are used iteratively. For the models discussed in this paper, sets of about 800 pseudorelative permeability curves are generated based on the across-fault flow rates at particular times in the simulation run (e.g. Fig. 7), and the simulator is then restarted using these updated functions. This process is repeated up to eight times over the field life, ensuring that the upscaled pseudorelative permeability functions are appropriate for the constantly changing reservoir conditions. The functions themselves are included in the simulation model as directional irreversible curves, implying that they are used only for flow across the fault connections in the specified directions (e.g. Fig. 7).

The results (Figs 3, 4) show modest reductions in oil production using the datum set of two-phase properties (Case 1), with a further decrease as a function of the modified capillary pressure curves (Case 2), and a much more significant effect if the oil relative permeability decreases at lower intrinsic fault permeabilities (Case 3). Given the scarcity of laboratory measurements of two-phase fault rock properties, it therefore appears that they can impart considerable uncertainty in production from faulted reservoirs. It is likely, however, that as more data are obtained the range of plausible input functions can be narrowed, thereby reducing the uncertainty range suggested by the results presented.

Effects of the spatial variability in single-phase permeability

The assumption made implicitly when using a single deterministic relationship between SGR and permeability is that the correlation length of permeability variability is considerably smaller than the size of a grid-block. The deterministic permeability therefore represents the arithmetic average of the heterogeneous distribution (Manzocchi *et al.* 1999). Since there is a paucity of geological data on correlation lengths of fault rock properties, this assumption may be wrong and its implications on production have been explored. Models with fault permeability varying stochastically over larger correlation lengths have been conditioned to random fields containing the standard normal distribution (i.e. with a mean of 0.0 and a standard deviation of 1.0). The random fields have been generated with Gaussian variograms using three different correlation length models. In each model the vertical correlation length is ten times smaller than the horizontal ones which are 300 m (Case 1; Fig. 8a), 1 km (Case 2, Fig. 8d) or 5 km (Case 3, Fig. 8b). Two different distributions of fault rock permeability have been considered for each correlation length, with fault rock permeability at a particular SGR assumed to be distributed

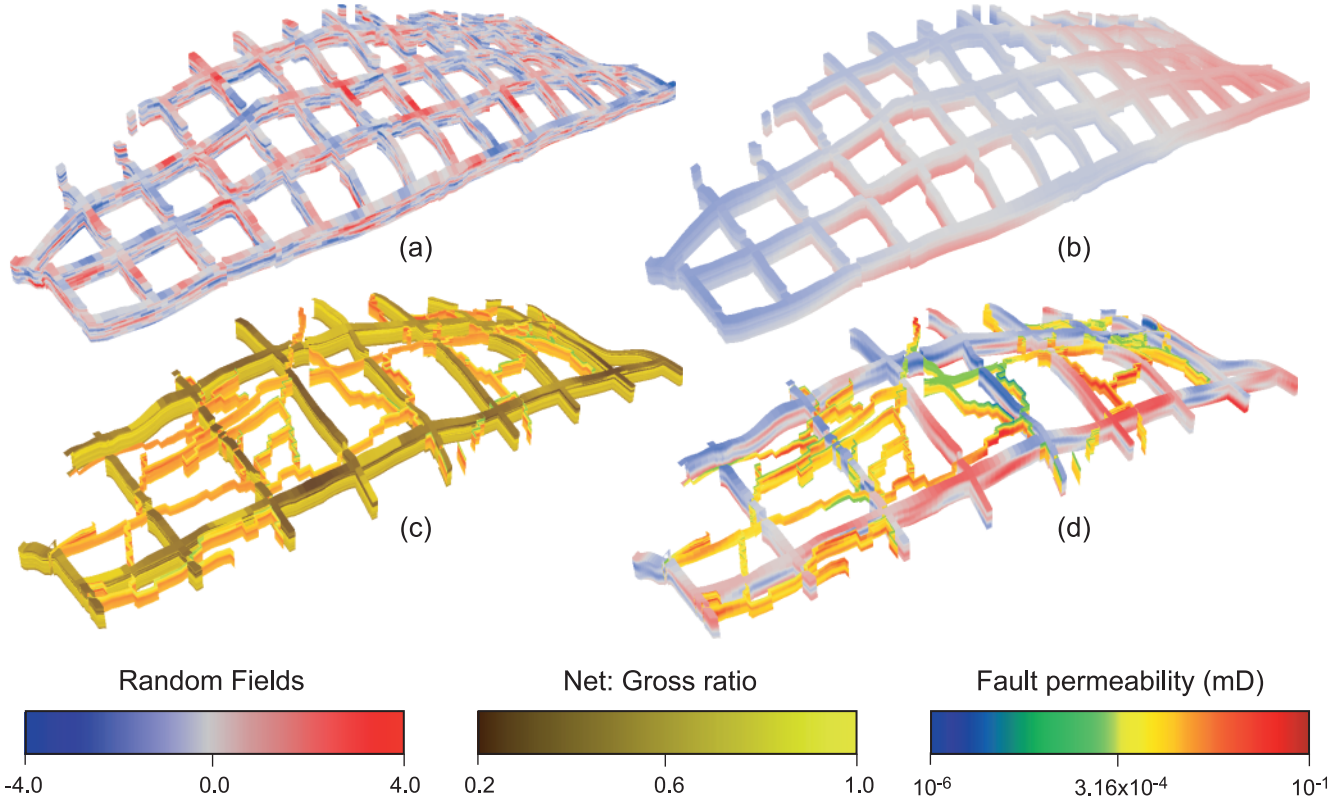

Fig. 8. Examples of the correlated random fields with horizontal correlation lengths of (**a**) 300 m and (**b**) 5 km shown for Structure B. (**c**) The deterministic fault permeability is a function of the fault throws and cell V_{shale} (in these models the net:gross ratio is used as a proxy for this). (**d**) Fault permeability modelled as a function of SGR but conditioned to the correlated random field shown (with a horizontal correlation length of 1 km) according to Case 2 (i.e. the standard deviation of $log_{10}k_f$ =1.0).

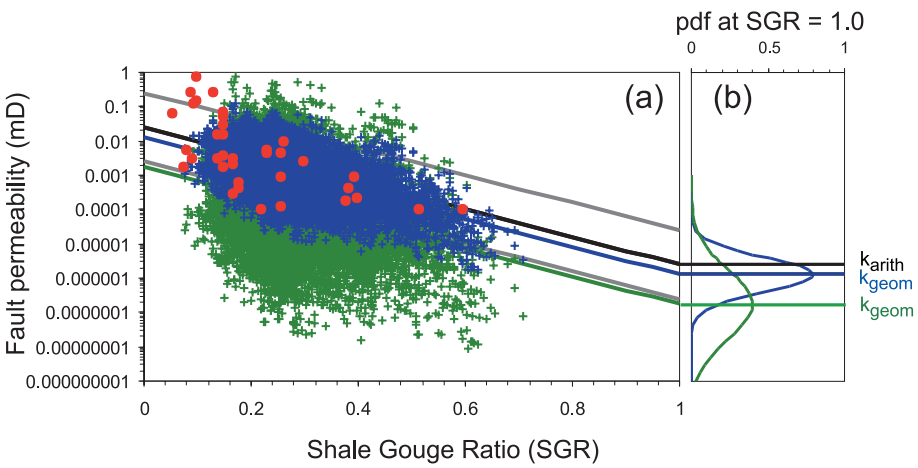

Fig. 9. (**a**) Realizations of fault connection permeabilities as a function of SGR for models using Case 1 (Blue) and Case 2 (Green). The red data show laboratory results for drill core samples of Brent Group reservoirs for burial depths in the range 3–3.7 km (from Jolley *et al.* 2007). The two grey lines show the deterministic reference cases one order of magnitude more, and less permeable than the datum case (shown in black). The green and blue lines show the geometric average relationships for the realizations. (**b**) Probability density functions for fault permeability extrapolated to SGR=1. Realizations have the same arithmetic average permeability as the datum case, but their geometric average (which corresponds to the median value at a particular SGR) is lower.

log-normally with a standard deviation of $log_{10}k_f$ of 0.5 or 1.0 (e.g. Fig. 9). The pre-processor combines the correlated random field with the deterministic fault permeability model to generate the final correlated permeability fields (e.g. Fig. 8d). The resultant permeability fields have the same arithmetic average permeability as the deterministic relationship (Fig. 8c) but, since k_f is assumed to be log-normally distributed, lower median values (i.e. geometric averages; Fig. 9b). Six realizations of each of these six distribution models were simulated on each structure (Figs 3, 4).

The influence on production of the different models (Fig. 4) shows some quite subtle effects. Oil production on average decreases relative to the datum models for Cases 1 and 2, and then increases again for Case 3. Accompanying this increase at the largest correlation length is a significant increase in the variability between realizations. The same overall trends are observed from both reservoirs and, unsurprisingly, are more marked when the modelled permeability distribution is broader. For the lower correlation length models, flow across particular faults is focused preferentially through the higher permeability regions, and the initial decrease in production reflects the presence of locally more poorly swept areas upstream of lower permeability regions. As the correlation length of the variability increases to approach or exceed the lengths of faults (in the non-compartmentalized Structure A reservoirs) or of compartment-bounding fault segments (for the Structure B

reservoirs), the faults themselves are less heterogeneous at smaller scales, which means that the effect discussed above is subdued. Instead, the average permeability of the fault or fault segment becomes the important control, and the range of behaviour is wider since it depends on whether the faults or fault segments that are critical to the flow paths have sampled the upper or lower portions of the overall permeability distribution.

FAULT THROW EFFECTS

Two distinct types of fault throw effects are considered. The first is uncertainty in interpreted fault throw. Possible errors in the interpreted throw are modelled using correlated random fields to mimic an uncertainty on throw of ± 10 m. The results are presented from six realizations each for three correlation lengths of possible error. The second fault throw effect considered is the inclusion of sub-seismic faults. Although the models are of synthetic reservoirs, both structures derive from seismic interpretation of natural fault systems (see Manzocchi *et al.* 2008*b* for details) and, like all models of natural reservoirs, they are therefore subject to resolution effects. Three realizations each of two sub-seismic populations are considered for each structure. The frequencies and sizes of the sub-seismic faults are conditioned to orientations and populations of the seismically resolved faults, but their locations are assigned randomly. The largest faults added have maximum throws of about 10 m and the smallest of 2 m (which is half of the height of the cells in the models). The effects of both juxtapositions and fault rocks (using the same SGR and throw dependencies as for the faults included explicitly in the model geometry) of the sub-seismic faults are included in the simulation models.

The results (Fig. 4) show that the effects on production of some of these representations can be severe and may impact production in both a positive or negative sense (or, in the case of the sub-seismic faults in the Structure A reservoirs, either positively or negatively depending on whether the oil production index considered is discounted or not; Fig. 4e). Before discussing geological and methodological details and results further, it is necessary to describe the basic method (which is termed geometrical upscaling) used to include in the simulation models both the fault throw effects described in this section and the fault zone effects described in the subsequent section.

Geometrical upscaling

The purpose of simulator fault property pre-processors is to calculate transmissibilities for each across-fault connection representative of the particular model of the fault rock present at each location (e.g. Fig. 10a). These transmissibilities are then included in the simulator using appropriate keywords defining multipliers on, or replacements for, the transmissibilities calculated by the simulator, which are a function only of the geometry and properties of the juxtaposed cells (e.g. Schlumberger 2005). For example, the transmissibilities of the stack of faulted connections shown in Figure 10b derive from the geometrical arrangement and properties of the two stacks of cells shown in Figure 10c, and from the modelled permeabilities and thicknesses of fault rock within this surface. In this particular example, each cell is connected to three cells on the other side of the fault (Fig. 10b). In Figure 10d the across-fault connections associated with the hanging-wall cell in layer 7 (i.e. the cell highlighted by thicker edges) are coloured by transmissibility values in the footwall cells they apply to. Hence, Figure 10d contains the same information as Figure 10b, but for only one of the footwall cells in the stack of cells.

Geometrical upscaling is referred to as the process of representing at the resolution of the simulation model the transmissibilities associated with a similar (but different) fault surface model or with a higher resolution fault zone model. In Figure 10e, for example, the throw on the fault shown in Figure 10d is reduced by 7 m. Given exactly the same fault rock permeability and thickness predictors, this has the effect that the hanging-wall cell in layer 7 is now connected to the footwall cells in layers 9 and 10 with the transmissibility values indicated by colour in Figure 10e. These connections and their transmissibilities can be represented in the original simulation model (which contains the geometry shown in Figs 10a–d) by: (a) resetting to zero the transmissibilities between the reference cell and footwall cells in layers 11 and 12 (since these connections do not exist in Fig. 10e); (b) redefining the connection transmissibility to footwall layer 10 (since this connection exists in both the original and revised model geometries); and (c) adding an entirely new connection (with the appropriate transmissibility value) between the hanging-wall cell in layer 7 and footwall cell in layer 9. That this final connection has no existence in the simulator model geometry (and therefore cannot be represented graphically in Fig. 10b) is irrelevant: if instructed to do so, the simulator will treat it in exactly the same way as any cell-to-cell connection that does exist. The procedure is applied to each layer in the model, and to each stack of across-fault connections that are modified.

The process discussed above technically is not upscaling since there is no difference in resolution between Figures 10d and e. However, the same basic approach can be used to represent three-dimensional fault zone geometries (including associated fault rock properties) within the lower resolution geometrical framework of the simulation model. Figure 10f, for example, shows the geometry that would be present were the single fault surface contained in the simulation model (i.e. Fig. 10d) actually to consist of a pair of slip surfaces each containing 50% of the total throw. The highlighted cell (i.e. hanging-wall layer 7) in this higher resolution model is connected physically to three layers within the fault-bounded lens. The transmissibility of each of these connections can be calculated as a function of the geometry and properties of the highlighted cell, of each narrow lens cell, and of the permeability and thickness of the fault rock in the fault segment that separates them. Each of the three cells in the fault-bounded lens, however, is also connected to one or more other cells on both the footwall and hanging-wall sides of the fault zone. The net result is that, via the fault-bounded lens, the highlighted cell is now connected to five cells on the footwall side of the fault (layers 9–13) and four cells on the hanging-wall side (layers 5, 6, 8 and 9). With the exception of the two cells immediately above and below the reference cell, the transmissibilities of each of these flow paths are indicated by colour in Figure 10f, and can be included in the simulation model using replacements, deletions and introductions of connection transmissibilities as discussed above. The reason for not including the transmissibilities associated with the two vertical neighbour connections is that these connections already exist in the parent model geometry and, except under very rare circumstances, flow paths in the fault zone have only a negligible effect on the transmissibilities (calculated by the simulator) between these cells.

A second fault zone example is shown in Figure 10g. In this case an unbreached relay zone is present on the fault, and many more cells are now connected to the highlighted cell than in the paired slip surface example (Fig. 10f). This increase is because the difference in dip of the ramp relative to the cells implies that each cell in the ramp is connected to more cells in both the footwall and hanging-wall cell stacks. The connection between

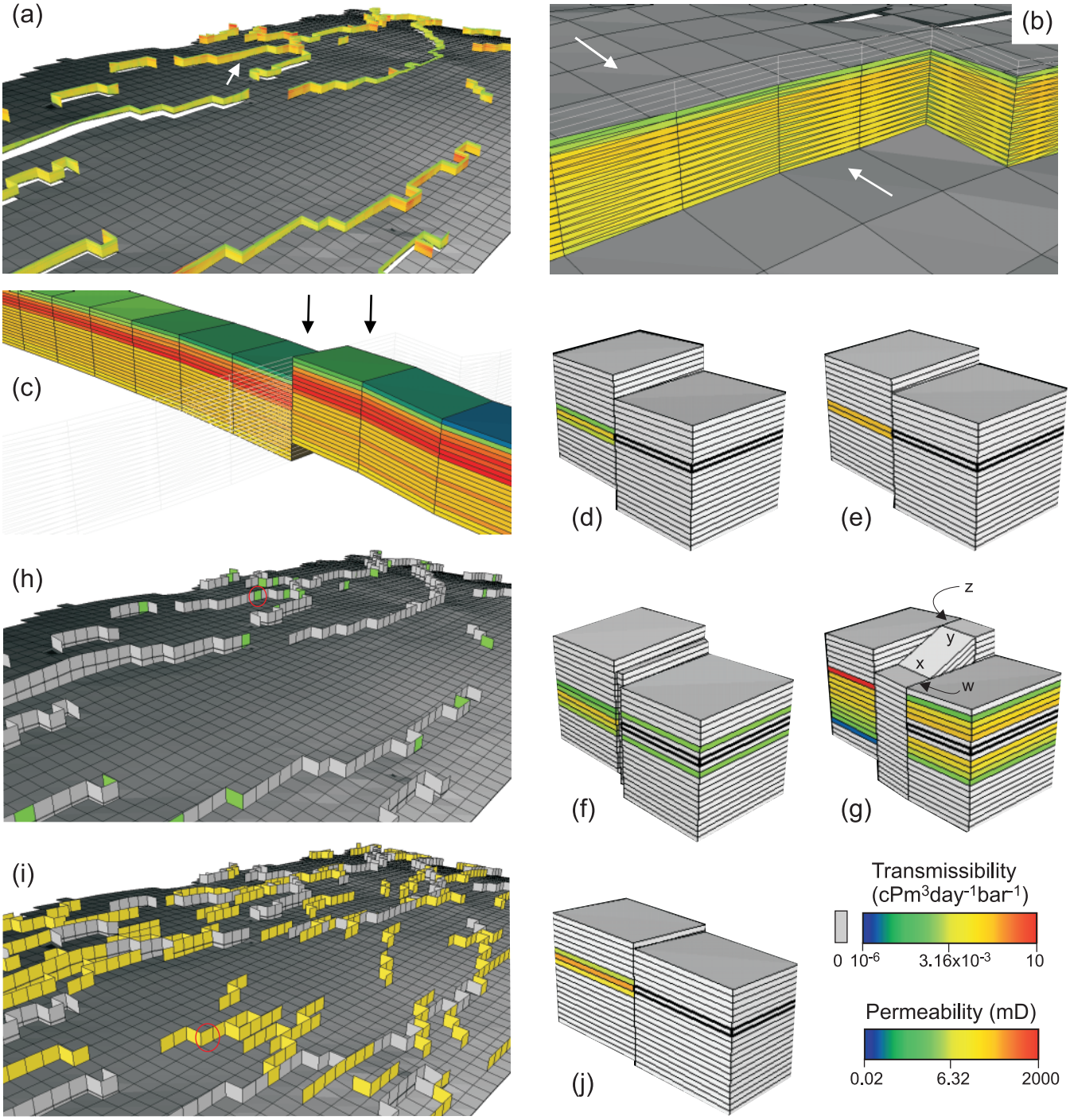

Fig. 10. Illustration of the geometrical upscaling method. (**a**) The datum across-fault transmissibilities for Reservoir A. (**b**) A close-up of the fault indicated by the arrow in (a). (**c**) A close-up of the row of cells indicated by arrows in (b), coloured by cell permeability. (**d**) The geometry of the two cell stacks indicated by arrows in (c), coloured by transmissibility for the cells connected to the one highlighted by thicker edges. (**e**) As (d), but for the situation where the throw on the fault is reduced by 7 m. (**f**) As (d), for the situation where the fault is represented by two closely spaced faults, each accommodating half the aggregate throw. (**g**) As (d), but for the situation where an unbreached relay ramp is present on the fault. (**h**) Locations of stochastically placed relays are shown in green for a realization of the low relay density case (Case 1). Note that the size of any of these ramps is a function of the local throw and does not cover the entire length of the fault face. The highlighted stack of fault connections is the one shown in (g). (**i**) Locations of sub-seismic faults added in a realization of the low-density case (Case 1) are shown in yellow. (**j**) Across-fault transmissibilities associated with the highlighted cell. This stack of cells is a close-up of the sub-seismic fault indicated in (i). See text for discussion.

the highlighted cell and the cell in layer 7 in the footwall has a much larger transmissibility than the others. This is because one of the many pathways through the relay zone between these two cells is the only across-fault pathway associated with the reference cell that does not pass through low permeability fault rock. In this example, the vertical planes labelled w, x, y and z on Figure 10g are drawn for clarity and do not imply the presence of faults. Hence, the flow path in question is through these four planes (within layer 7). Discrete fault offsets can be included on one or both of the x and y planes if instructed

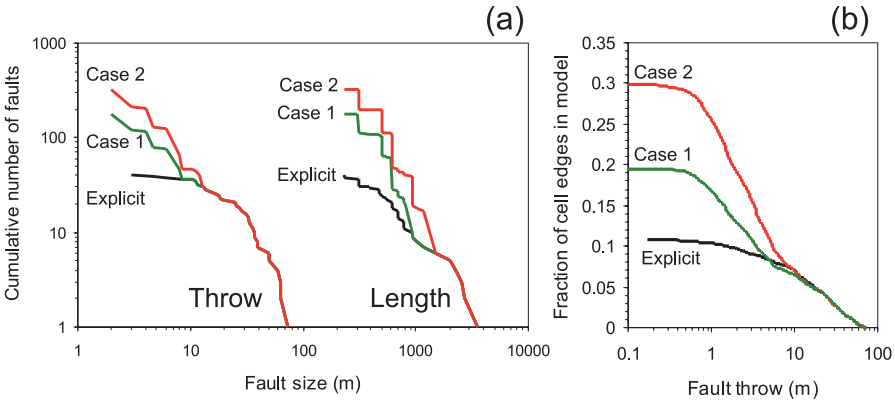

Fig. 11. (**a**) Fault throw and length populations for the deterministic Structure A reservoir (black) and for realizations of the low (green, Case 1) and high (red, Case 2) sub-seismic fault density cases. (**b**) Fraction of horizontal cell edges in the model offset by faults of specific sizes for the cases shown in (a). Population curves are the same at throws >10 m and at lengths >1500 m.

(Fig. 10g), in which case the relay would be singly or doubly breached and no flow paths through it, avoiding faults, would be possible. Flexible input of the fault zone geometry allows the inclusion of a continuum of structures ranging between the two shown (Figs 10f, g) as well as others, allowing transmissibilities associated with realistic models of fault zone geometries to be included in the simulation model without the need for local grid refinements. The flow properties of the lens or ramp cells (Figs 10f, g) are inherited from their source cells, but may be modified subsequently to represent damage. Additionally, the properties of the cells themselves can be modified locally to reflect damage in the walls of the fault. Models using both types of modification are described in the following section.

The discussion above has centred on the method applied to faults that exist explicitly in the geometry of the simulation model; however, exactly the same approach can be applied where no fault is present. For example, Figure 10i shows in yellow the locations of cell edges that are not fault-bounded in the simulation model, but have been assigned fault offsets in the pre-processor to represent a possible population of sub-seismic faults. The offset associated with the highlighted cell edge in Figure 10i is shown in Figure 10j. In this example, the highlighted cell is connected to three cells in the footwall, but only one of these connections exists explicitly in the model geometry. The transmissibility of this connection is lowered to reflect the reduced juxtaposition area and presence of fault rock in the higher resolution model (Fig. 10j), and the transmissibilities of the other two connections are added to the simulation input deck. Using pre-processor output files generated in this way, the overall geometry of the simulation model does not need modifying to include fully both the juxtaposition and fault-rock effects of the sub-seismic faults.

Effects of uncertainty in fault throw

The automated methods discussed above provide an easy means of including in a version of the simulation model effects of high frequency throw variations, of general uncertainty in throw, or of more targeted throw interpretation ambiguities. The first two of these are examined, by applying globally a 10 m uncertainty on fault throw. The procedure used is fairly similar to that used to model the correlated fault permeability variations discussed in the previous section. A series of correlated random fields (in this case two-dimensional) are used to condition the distribution in throw error. These have correlation lengths of 300 m (Case 1), 1 km (Case 2) and 5 km (Case 3). The error in throw is assumed to be distributed normally, with a mean of 0 m and a standard deviation of 10 m. This implies that throws are just as likely to increase as decrease from those contained explicitly in the model, and that along 38.3% of the fault lengths, throws will be within 5 m of their explicit value, and along 68.3% of the length they are within 10 m. The distribution implies that throws will be altered locally by 20 m or more over about 5% of the trace length.

The simulation results for these cases more or less mirror those for the cases with correlated variability in fault permeability (Fig. 4). Progressive increases in oil recovery are shown for Cases 1 and 2, which then reduce (on average) for Case 3, accompanied by a large increase in variability among individual realizations. The increased oil production for the low correlation length models can be attributed to a beneficial effect overcoming two detrimental ones. The beneficial effect is that high frequency throw variations mean that individual faults or compartment-bounding segments are more likely to contain favourable juxtapositions through which flow can be focused preferentially. This will tend to increase production rates at the expense of sweep efficiencies. The first detrimental effect is the reduction in sweep efficiency alluded to above. The second is that there is slightly more fault rock present in these models overall than in the datum model, since a fault which has an explicit throw of less than the modelled local error (and if this local error decreases the throw) will reverse its displacement sense. At larger correlation lengths the average behaviour of the realizations is similar to the datum model for both structures, but the wide range of responses is a reflection of whether or not the modified throws on the critical faults or fault segments are more or less favourable to production than they are in the deterministic case.

Effects of sub-seismic faults

Two models of sub-seismic faults are considered and three relaizations are used for both. In these cases the populations of faults present explicitly in the simulation model are extrapolated to smaller throws using length-to-throw ratios representative of the larger faults (see Manzocchi *et al.* 2008*b*, for details of the fault populations represented explicitly in the simulation models). Two extrapolation models are used (e.g. Fig. 11a) and the locations of faults in one of the lower density (i.e. Case 1) realizations is shown for Structure A in Figure 10i. The sub-seismic faults result in an approximate doubling (Case 1) or trebling (Case 2) of the number of faulted cell edges in the models (Fig. 11b). However, since they have small throws, the total fault rock present in the reservoirs is increased by only about 4% (Case 1) or 20% (Case 2). The faults are placed randomly with orientations conditioned to the orientation of the explicit faults, and their juxtaposition and fault rock effects are included using the methods discussed above.

The sub-seismic faults have a much larger effect in Structure A, where they show counterintuitive increases in total oil

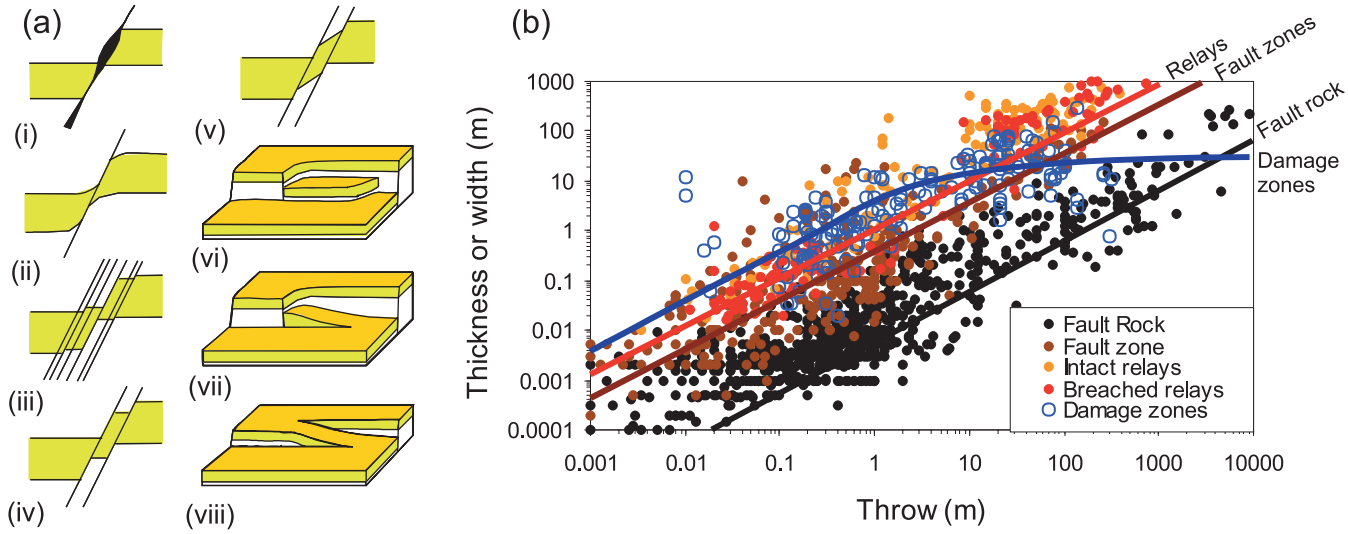

Fig. 12. (**a**) Cartoons of fault zone complexities: (i) fault rock; (ii) normal drag zone; (iii) damage zone; (iv) paired slip surfaces; (v) paired slip surfaces with a rotated fault lens; (vi) fault lens; (vii) singly-breached relay zone; (viii) intact (i.e. unbreached) relay zone. (**b**) Compilation of field measurements coloured according to identifiable fault zone structure. The black, brown and red lines indicate the scale-independent models used in this work for fault rock thickness (this is representative of the harmonic average of the distribution; Manzocchi *et al.* 1999), for paired slip surfaces and for unbreached fault relay zones, respectively. The blue line is the scale-dependent relationship used for the damage zones. See text for discussion.

production but decreases (particularly significant for Case 2) in discounted production (Fig. 4). Following the arguments of Manzocchi *et al.* (2008*b*), these trends can be rationalized by considering the effects of the faults on sweep efficiency (which they will increase) and flow rate (which they will decrease). Total recovery depends chiefly on the former and thus increases, while discounted recovery relies more on the achievable flow and thus decreases. These effects are manifest in Figure 3a, where the lower than average production rates in the first ten years are compensated by higher than average ones in the final twenty years. These reservoirs have become compartmentalized by the higher density sub-seismic fault cases (Case 2) and, although their production is not as poor as for the Structure B reservoirs (since the compartmentalizing faults are small and therefore have narrower fault rocks), their production profiles (Fig. 3a) tend towards the more linear profiles obtained in the bulk of the Reservoir B models (Fig. 3b).

The Structure B reservoirs containing sub-seismic faults show only very modest changes with respect to the datum case (Fig. 4). This is because these reservoirs are already compartmentalized, and the amount of fault rock added to the system is small compared to that present in the datum model. Hence, the preferred flow paths in these reservoirs are neither altered nor impeded significantly. This contrasts with the Structure A reservoirs, since tortuous flow around faults provide the preferred flow paths for these low fault permeability models, and the potential for tortuous flow is disrupted (Case 1) or negated (Case 2) by the sub-seismic faults.

FAULT ZONE EFFECTS

The previous sections have described results from simulation models addressing the assumptions that fault rock permeability can be represented adequately by a particular deterministic function ignoring two-phase properties; and that the fault throw included explicitly in the simulation model geometry is correct and sufficient. This section focuses on the geometry of the throw distribution within the fault, by concentrating on the assumption that the fault throw used to derive across-fault transmissibilities is accommodated within a single slip surface containing a discrete thickness of fault rock. This is known to be a massive simplification of the complex 3D structure associated with faults, and various conceptual models rationalize aspects of this complexity with varying degrees of success (e.g. Caine *et al.* 1996; Childs *et al.* 1996; Walsh *et al.* 2003*a*). The conceptual model used in this work is summarized schematically in Figure 12, using cartoons of idealized fault geometries (Fig. 12a) referenced to a recent compilation of fault measurements (made perpendicular to the fault strike) indexed to overall fault throw (Fig. 12b).

The assumption generally made in flow simulation modelling is that the cell offsets represent a single, planar fault, containing a discrete thickness of low permeability fault rock (Figs 12a, i). This simplistic fault model is observed very seldom at outcrop, and natural faults generally exhibit some or all of the geometrical complications shown schematically in Figures 12a ii–viii). Often a fault is surrounded by a distributed zone accommodating part of the overall fault offset. The strain in this region may either be accommodated by ductile deformation manifest as a normal drag zone (e.g. Fig. 12a ii), through brittle faulting, in which case it is generally referred to as a damage zone (e.g. Fig. 12a iii), or through a combination of the two (e.g. Hesthammer & Fossen 2000).

Most of the offset in natural faults is accommodated in a narrow zone within this normal drag/damage zone, but usually not on a single through-going planar structure as implied by Figure 12a i–iii. Instead, two discrete slip surfaces accommodating a significant fraction of the overall offset, and bounding a more or less deformed zone of wall-rock, are frequently observed (e.g. Fig. 12a iv). Such throw partitioning may strongly modify the flow geometry associated with the fault, since multiple slip surfaces do not result in the same juxtapositions as one surface containing the aggregate throw (e.g. Fig. 10f; Childs *et al.* 1997; Hesthammer & Fossen 2000), particularly if bed rotations in the fault-bounded lenses also occur (e.g. Fig. 12a v). The multiple-slip surface geometry shown in Figure 12a iv could derive from a cross-section through the centre of any of the three block diagrams in Figure 12a vi–viii, which show a fault-bounded lens (vi), and singly-

breached (vii) and unbreached (viii) relay zones. Clearly the across-fault flow implications of these structures are vastly different, implying that conceptual models of fault zone structure, if applied to flow issues, must be three-dimensional as a basic prerequisite.

Figure 12b indicates the existence of a continuum of geometrical fault zone complexities on faults of particular sizes ranging from fault rock through more or less damaged fault zones (the requirement for defining a fault zone in Fig. 12b is the presence of recognizable wall rock within a zone bounded by discrete, kinematically related, synthetic slip surfaces) through to more systematic structures with the recognizable geometry of breached and unbreached relay zones. The generation and evolution of these structures within a growing fault are beyond the scope of this paper and will be discussed elsewhere. The present paper is concerned with establishing and applying quantitative descriptions of them, so that the effects of realistic fault zones on oil production may be determined in these example reservoir models. Three different effects are considered and, in each case, the revised transmissibilities associated with the changes in fault model are included in the simulation models using the geometrical upscaling approach described in the previous section. The first effect considered comprises a range of deterministic parameterizations of brittle fault damage zones or ductile normal drag zones (e.g. Fig. 12a ii, iii). In these models, the zones are expressed by functions defining: (a) the fraction of fault throw taken up by minor faults or ductile drag around the main fault; (b) the width of the damage zone; (c) the total thickness of faults in the damage zone; and (d) the permeability of the damage zone faults. In the second set of models, different proportions of the total fault lengths are assumed to comprise paired rather then single slip surfaces (e.g. Figs 10f, 12a iv). The third set of models comprises four parameterizations of relay zones placed stochastically on faults according to different models of relay frequency and damage (e.g. Figs 10g, 12a viii).

Effects of normal drag and damage zones

The effects on production of localized zones around the faults containing minor faults and/or accommodating a portion of the fault throw are addressed through three deterministic fault models applied to each structure. Case 1 includes only changes to the fault properties and juxtapositions arising from local normal drag zones. Case 2 includes only the effect on equivalent fault permeability of an explicit damage zone of low permeability faults. Case 3 includes both effects.

The model of local normal drag assumes that the planar fault surface included in the simulation model comprises a portion of the throw taken up by ductile normal drag. The conceptual model behind the equation used to model the resultant reduction in localized fault throw is that a fault is initially manifest as a distributed region containing no discrete fault surfaces longer than the scale of a simulator grid-block (i.e. in these examples, 75 m). Only once the fault throw accumulates beyond a particular throw threshold does it localize onto a single, through-going surface, and subsequent growth is accompanied by a progressive reduction in the fraction of the total throw accommodated by ductile processes around the fault. The equation used to model this effect is $d'_f = d_f(1-(2d_f)^{-1})^{40}$, where d'_f is the modified throw used to redefine juxtapositions and calculate transmissibilities, and d_f is the throw explicitly included in the model. The function implies a pre-localization offset of 0.5 m accommodated by normal drag. With a 10 m aggregate throw (d_f), the localized throw (d'_f) is 1.3 m and 40% of the incremental throw is accommodated on the localized fault surface. With a 25 m aggregate throw, the localized throw is 11 m and only 20% of the incremental throw is accommodated by normal drag. This rather severe model is put into context by examples such as the one discussed by Hesthammer & Fossen (2000), who described a 100 m offset fault in which only 9 m of the total throw is accommodated on a discrete slip surface; the remainder is accommodated by ductile normal drag within a zone extending *c.* 100 m on either side of the fault.

The effects of a damage zone comprising minor faults around the main surface are included in the simulation models using a quantitative parameterization based on field observations. The damage zone width (t_{dz}) is assumed to be related to the throw on a fault according to the expression $t_{dz}=30x^{\exp(-x)}$, where $x=(\log_{10}(d_f+1))/3)$. This relationship is based on the field measurements shown in Figure 12b (Beach *et al.* 1999; Hesthammer & Fossen 2000; Shipton & Cowie 2001) and is compatible with the normal drag expression used above, since it implies a linear increase in damage zone thickness with increasing throw up to a throw of *c.* 0.5 m, followed by a gradual deceleration of damage zone expansion as the fault becomes more localized. The volumetric fraction of the damage zone comprising low permeability fault rock (gouge density; d_G) is calculated as a function of the cell porosity using the expression $d_G=0.1\phi^{1.5}$. This expression results in $d_G=1.6\%$ in a 30% porosity rock, comparable with values observed close to large faults in high porosity sandstones by Antonellini & Aydin (1994; see also Manzocchi *et al.* 1998 for a discussion of realistic d_G values). The permeability of faults in the damage zone is estimated using the same expression as used in the rest of the modelling, and by assuming that their SGR is equal to the V_{shale} of the cell in which they are contained. The V_{shale} of the best quality facies present (i.e. the upper shoreface) is *c.* 0.15, hence the permeabilities of the damage zone faults in this facies are about 0.005 mD; i.e. five orders of magnitude lower than the undeformed grid-blocks. The permeability contrast in the poorer quality facies is less severe. The effects of the damage zone are implemented in the pre-processor by modifying the fault rock permeability so that it also includes the reduction in equivalent cell permeability arising from the adjacent damage zones. The damage zones result in a net reduction in equivalent fault rock permeability of between about 20% and 95%, with the largest reductions observed on smaller throw faults adjacent to less clay-rich cells (Fig. 13).

Simulation results show that these effects can influence oil production quite significantly, particularly for Structure B (Fig. 4). The models including only deterministic drag (Case 1) increase production by an approximately equivalent amount as increasing all fault permeabilities by a factor of 10. The case including only the damage zones (Case 2) lies approximately midway between the datum case and the case with permeabilities a factor of 10 lower, comparable with the observed decrease in effective fault permeability (Fig. 13). When both factors are included (Case 3) they are either beneficial or neutral with respect to the datum case.

In Structure B, the production profile for Case 1 is among the group of outliers (including some of the relay cases as well as the deterministic case with permeabilities one order of magnitude higher) with much higher production rates (Figs 3c, d). The normal drag function applied means that faults with throws up to 9 m have localized throws of less than 10% of their aggregate throw. In Structure B, most of the critical fault segments contain areas in which the fault throw is less then 9 m and, therefore, flow paths between compartments exist for which the modified fault throw is less than 10% of the throw in the deterministic model. Since fault rock thickness scales

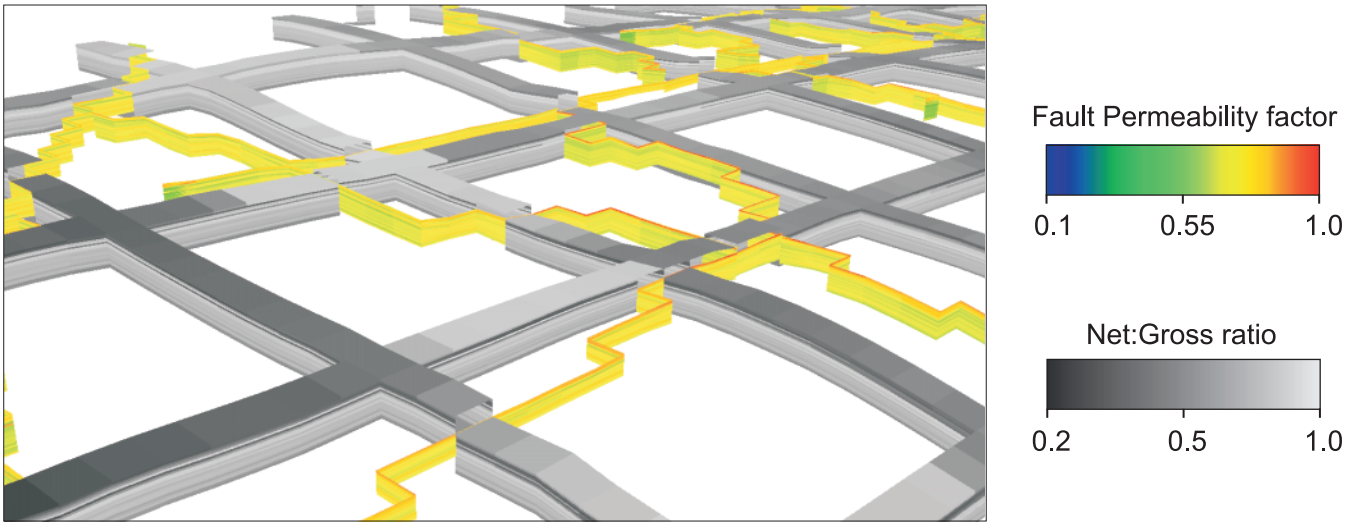

Fig. 13. Reduction in fault permeability when the effects of damage zones adjacent to faults are included as equivalent properties within the fault rock permeability.

linearly with fault throw, and because a reduction in fault rock thickness by an order of magnitude has the same effect on transmissibility as an increase in fault rock permeability by the same amount, inter-compartment flow paths in Case 1 are controlled by similar fault rock effects as they are in the deterministic case with faults one order of magnitude more permeable. Hence, the production profiles for these cases are similar (Figs 3c, d, 4f). For Case 3, the presence of the damage zone provides sufficient impairment for the production profile to fall within the main cluster of profiles (Figs 3c, d), despite the reduced fault throws and, although this case has a similar total recovery to the Case 1 model (Fig. 4), production from the latter occurs much more quickly.

Effects of paired slip surfaces

Two models containing paired slip surfaces are considered. In Case 1, faults are assumed to comprise single slip surfaces over 70% of their length, and paired slip surfaces over 30% of their length. In Case 2, these percentages are reversed. The locations of the paired slip surfaces are chosen at random, and the total throw is always assumed to be accommodated equally between the two (e.g. Fig. 10f). The horizontal distance between the two faults influences the transmissibilities and is modelled as a function of aggregate throw (Fig. 12b). The results for three realizations show modest increases in production for both fault systems (Fig. 4).

The geometrical model used to define the fault lenses in these realizations is geometrically rather simplistic, since it does not include rotations parallel to either the fault strike or dip. Inclusion of these additional fault zone properties would result in a range of production profiles with end-member cases similar to the deterministic normal drag cases discussed above for rotations parallel to fault strike (Fig. 12a v), and to the cases with unbreached fault relay zones discussed below for rotations perpendicular to fault strike (e.g. Fig. 12a viii).

Effects of fault relay zones

The degree of segmentation within a particular fault system is attributed generally to strong rheological contrasts and heterogeneities within the rock volume containing the propagating fault, and to the orientation of the fault with respect to the regional extension direction and bedding orientation (e.g. Mandl 1987; Childs *et al.* 1995, 1996; Huggins *et al.* 1995; Walsh *et al.* 2003*a*; Schöpfer *et al.* 2007). The objective in the present work is not to attempt to derive an equation linking the degree of fault segmentation with all its possible causes, but to identify a simple function allowing realistic segmentation (manifest in these examples as unbreached relay zones) to be included within the continuous fault surfaces contained in the simulation models. The fundamental observation guiding this function is the requirement for fault traces with larger throws to contain fewer, but larger relays.

The expression used in the modelling is $f=Bd_f^{-1}$ where f is the frequency of relays (number per metre) on a fault with throw d_f. The expression is applied stochastically in the reservoir simulator pre-processor, which calculates the probability that each stack of faulted cell edges contains a relay based on consideration of the local throw and the length of the relevant edge of the faulted cell stack. Once a relay has been assigned at a particular location in the model, its dimensions (width and length) are also assigned as a function of the local throw. The present study uses ratios of 1:1 between throw and ramp width, and 2:1 between ramp length and throw to give relay zones representative of natural examples (e.g. Huggins *et al.* 1995; Imber *et al.* 2004; Soliva & Benedicto 2004). An example realization generated using B=0.01 is shown in Figure 10h, with the geometry of one of the ramps shown in Figure 10g.

Figure 14 contexturalizes the relay frequency model against natural data. Since the model includes linear dependencies between fault throw and both the frequency and geometry of the relays, it is scale independent. Figure 14a shows sets of idealized trace maps scaled to different fault throws at two different values of B. These maps can be compared to natural systems (e.g. Fig. 14b, which shows a horizon coherence slice of a highly segmented system of intraformational faults; see Bailey *et al.* 2003, for details) to give a semi-quantitative impression of what frequency constant B might be. Segmentation in Figure 14b appears to be representative of $B\approx0.04$. Figure 14c compares the populations of relays modelled in three realizations of the two constants used on Structure A with those obtained from outcrop or seismic interpretation. The natural examples show approximately power-law relay populations down to a vertical and lateral cut-off value determined by the resolution of the data. The relays in the simulation models are smaller since they are below the resolution of the seismic

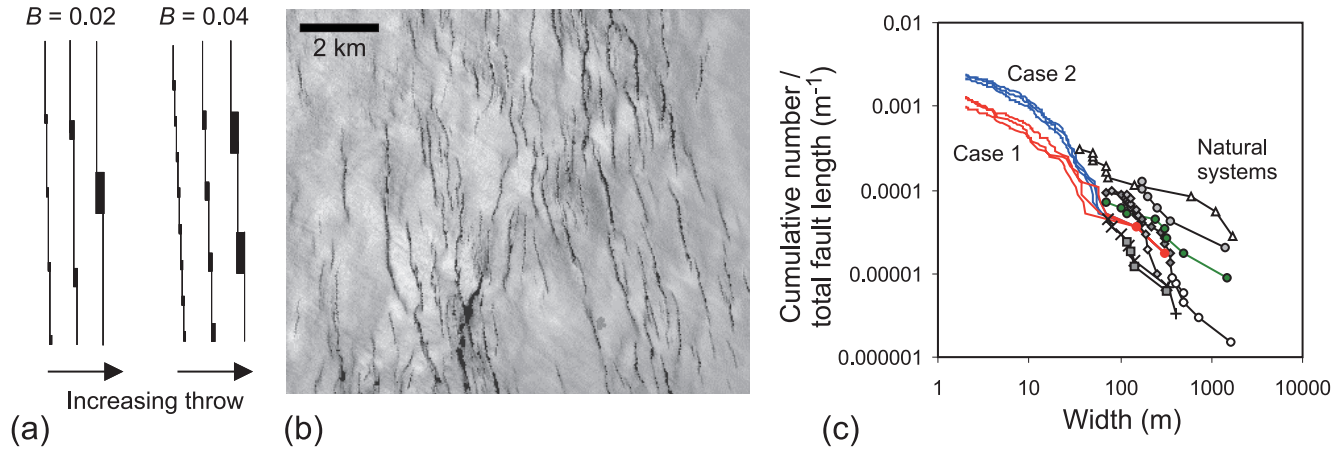

Fig. 14. (**a**) Scaled fault trace maps of relay populations modelled according to characteristic throw: length and throw: width ratios and the two frequency constants (*B*) indicated. (**b**) Horizon continuity map for intraformational faults in the Porcupine Basin (after Bailey *et al.* 2003). (**c**) Populations of natural relay zones interpreted from seismic and outcrop examples (black and green), compared with three realizations of the low (Case 1, red curves) and high (Case 2, blue curves) relay frequency models applied to the Structure A reservoirs. The two relays large enough to be represented explicitly within the model (Fig. 2a) are shown as red dots and define the upper end of these populations. The green data derive from a larger-scale analysis of the fault system upon which Structure A is based (e.g. Walsh *et al.* 2003*b*). See text for discussion.

data but fall within the same envelope, implying that the values of *B* used in the modelling are representative of natural fault systems.

Three realizations each of four cases were applied. In Cases 1 and 2 the relay zone permeabilities are identical to the cells they derive from, and frequency constants (*B*) of 0.01 and 0.04 define low and high segmentation cases, respectively. Cases 3 and 4 both contain the high segmentation case, but the ramps are assumed to contain minor faulting resulting in a one order of magnitude (Case 3), or two orders of magnitude (Case 4) reduction in equivalent permeability in both the along-ramp and across-ramp directions; these are similar magnitudes of damage to those calculated for the Delicate Arch ramp in Utah by Rotevatn *et al.* (2007). Production results (Fig. 4) show that these realistic relay populations can have a very significant influence on production, particularly on the compartmentalized (in its deterministic non-segmented state) Structure B reservoir. The models containing higher relay frequencies perform better than the lower frequency ones, irrespective of whether or not the ramps are damaged. What is surprising is that the models containing moderately damaged ramps (Case 3) perform about as well as (Structure A) or perhaps even better than (Structure B) the models with equivalent densities of undamaged ramps (Case 2). This is because up-ramp flows are impeded sufficiently in the damaged models such that the compartments downstream of them are better swept as relatively more flow is obliged to pass through the portions of faults that do not host relay zones.

DISCUSSION AND CONCLUSIONS

The first objective of this work was to discuss effects on production of a broad range of issues associated with fault-related uncertainties and simplifications applied in reservoir simulation modelling programs even when a sound geological basis is used for across-fault transmissibility calculations. Results show that many of the factors considered, which are based on plausible geological descriptions, can impact field production significantly.

Cross-plots of discounted versus non-discounted total oil production (Figs 4e, f) show approximately linear trends for both structures, with many of the same cases occupying similar relative positions. On the whole, the fault-related alterations are much more significant for the compartmentalized Structure B reservoirs than for the Structure A ones, with the latter tending to have higher discounted recovery for the same total recovery (Fig. 4f), reflecting their higher initial production rates (Fig. 3). There are, however, some notable outliers. These are the sub-seismic fault cases which have lower than average discounted production for their total recovery in Structure A (Fig. 4e), and the normal drag and some relay cases for Structure B, which show the opposite. The plots also show that increasing fault rock transmissibility and increasing fault system segmentation have different effects on the two structures. In Structure A, an increase in fault rock transmissibility (reflected in the more permeable reference case and Case 1 from the damage zone/drag set of models) results in similar recovery but higher discounted recovery compared to the datum case. Structure A models with greater segmentation (i.e. the relay cases) are the best performers on the same trend as the bulk of the models (Fig. 4e). In Structure B, however, both these effects have a similar influence on production and the more segmented relay models as well as the two models with greater fault rock transmissibility are contained in the same group of Structure B outliers which are representative of the production behaviour of the Structure A reservoirs rather than the rest of the Structure B ones (Fig. 4f).

The behaviour of each model can be explained; however, because the production characteristics show inconsistent and quite complex dependencies on the fault-related parameters, it is unlikely that they could all have been predicted. Overall, therefore, it is considered that the results demonstrate the difficulty of generalizing on what the effect of a specific fault-related alteration might be. The two example reservoirs used in this study are very similar (they have identical sedimentological models, fluids, production mechanisms, volumetrics, over-all reservoir geometry and deterministic fault property predictors), yet the same modification has sometimes had very different effects. Reservoirs with entirely different geological or production-related characteristics may show vastly different sensitivities to the same fault-associated modification as the reservoirs used here. Moreover, even once the overriding controls have been established, it is still impossible to reliably second guess the influence of specific modifications, and intuition does not necessarily help. The models with moderately damaged relay zones, for example, have higher recovery factors

than those containing undamaged relay zones, and the models containing sub-seismic faults have higher recovery factors than those that omit them. Neither of these results is intuitive and sensitivity modelling therefore seems to be the only reliable means of assessing the significance of many fault-related production effects.

The second objective of this work has been to discuss methods for applying these generally neglected fault-related uncertainties in routine full-field production simulation. The approach used in the pre-processor described in this work is to represent the fault-related features at the resolution of the full-field flow simulation model, rather than by using local grid refinements. This approach is at odds with other ongoing research in which local grid refinements are preferred for the representation of, for example, fault zone structure (e.g. Syversveen *et al.* 2006) or two-phase fault rock properties (e.g. Berg & Øian 2007). Although different groups of workers may apply different geological idealizations of faults to define either the content and structure of the locally refined grids or the input to an upscaling solution, the overriding aim is identical: to represent more accurately the flow implications of fault-related geological heterogeneity. A flexible pre-processor should be capable of including different conceptual fault heterogeneity models provided that they are parameterized appropriately. The difference between the approach here and others is therefore fundamentally a practical engineering decision. It is not in contention that a more accurate solution should be obtained if a well-designed discrete grid is used, and high resolution flow modelling will always be required to validate fault-related upscaling methods (e.g. Manzocchi *et al.* 1999, 2002). However, given that the critical heterogeneities, even within large-displacement faults, are often on sub-millimetre scales, representing discretely the fault zone structure whilst minimizing numerical dispersion is likely to increase massively the number of cells in a model, and realistic three-dimensional heterogeneity in a fault through a layered sequence cannot be represented in a refined grid only dozens of cells wide. Some degree of upscaling will always be necessary. The most pragmatic approach is to upscale directly to the scale of the full-field flow simulation model, allowing effects of fault-related uncertainties to be assessed within the same simulation grid as other geological variables for which the requirement for upscaling is not questioned (e.g. lamina-scale sedimentary structure, which can have a large impact on production).

Establishing fault rock, fault throw and fault zone sensitivity models appropriate for particular fields relies on field-specific data and interpretations, and may result in quantitative models of the kinds of effects considered in this paper, but with different underlying dependencies and formulations. The fault-related parameterizations applied in this paper have been derived from general geological considerations, conditioned – where available – to quantitative public domain data. However, neither the range of uncertainties considered, nor the exact manner in which they have been modelled, are necessarily suitable to any particular field. For example, Hesthammer & Fossen (2000) discussed appropriate uncertainty models for the faults in the Gullfaks Field, including, among other things, depth dependencies on the properties of faults within damage zones. Provided the pre-processor to the reservoir simulator is sufficiently flexible to allow case-specific instructions, the effects of this (or other) dependencies can be included readily in the simulation model. Similarly, there is no reason why the properties modelled stochastically should not include deterministic components, or *vice versa*. Kinks in fault traces, for example, are often associated with breached or unbreached relay zones below the resolution of the seismic data. If a few relays are believed to be at particular locations on particular faults in the model, then they should be placed there deterministically, perhaps (but not necessarily) in conjunction with stochastic placement of other relays.

The same parameterization of stochastic throw uncertainty has been applied across all faults in the models; but in many instances the interpreter may be faced with ambiguous choices across only particular faults, in which case deterministic throw modifications targeted only to these faults should be applied. Similarly, a small fault omitted from the simulation model might be inferred from the production behaviour or identified by later inspection of the seismic volume. The precise location and throw of this fault should be added to the model deterministically, using the same procedures applied stochastically to model the sub-seismic fault populations. Conversely, the juxtaposition and fault rock effects of a fault included explicitly in the simulation model geometry should be replaced with unfaulted equivalents if it is decided that the fault does not actually exist. Combining these two approaches allows an assessment to be made of the sensitivity to uncertainties in fault locations.

The focus of this study has been on faults that are large enough for explicit representation at the resolution of the simulation model (these will generally be those that are resolvable seismically; however, as in the models examined, larger sub-seismic faults can sometimes also be included explicitly). Small-scale sub-seismic fault arrays have been considered in this paper only when they are spatially associated with large-scale faults (in these examples either as damage zones surrounding faults or within a damaged relay zone). However, clusters of deformation bands isolated from seismically resolvable faults may also influence reservoir-scale flows if the faults are low permeability and if the array is sufficiently well connected or strongly anisotropic (e.g. Manzocchi 1997). As a rule, deformation band arrays with permeabilities greater than about three orders of magnitude lower than the rock in which they are contained do not significantly influence equivalent permeabilities. This is because deformation band clusters are generally at least an order of magnitude less dense at scales relevant to full-field flow simulation (i.e. the scale of a grid-block) than the 20% volume fraction chosen to discuss their significance by Sternlof *et al.* (2004).

Another important aspect not discussed in this paper is the choice of fault rock property predictor, since the focus here has been on less conventional sources of uncertainty. In all the models presented, the same deterministic relationship between fault rock thickness and fault throw has been used, but fault rock thickness could be varied using similar approaches to those used for fault rock permeability. Fault permeability is often characterized using rather more dependencies than thickness, and different property algorithms are preferred for faults formed in different host rocks or under different conditions. Even when a particular algorithm is used, it may have a different formulation in different companies (e.g. compare the definitions of Clay Smear Potential; CSP, given by Fulljames *et al.* (1997) with that given by Yielding *et al.* (1997)), and some companies favour their own proprietary algorithms which may or may not be variants on public domain ones. A generalized form of all common equations is given by:

$$FSP = \sum_{First\ cell\ face}^{Last\ cell\ face} Throw^{L} Thickness^{M} Distance^{N} Effective V shale^{P} \quad (1)$$

where different values of the exponents L, M, N and P define the fault surface proxy-property (FSP). For example, setting

L=−1, M=1, N=0 and P=1 results in FSP=SGR. Setting L=0, M=2, N=−1 and P=0 gives FSP=CSP; but different options are needed to define the distance term and how the summation is performed to determine whether this CSP is equivalent to the algorithm of Fulljames *et al.* (1997) or Yielding *et al.* (1997). Setting L=1, M=−1, N=0 and P=0 gives FSP=SSF (Shale Smear Factor; Lindsay *et al.* 1993). Other exponents can give more specialist algorithms, for example dimensionless, V_{shale} and distance-weighted hybrids of SGR and CSP. Flexibility in the pre-processor can, therefore, be included by applying this generalized equation, and by allowing different FSP measures to be used on different faults in the same model, or a number of FSP measures to be used sequentially on the same faults (e.g. CSP might be used to model transmissibility barriers for continuous shale smears, followed by SGR to determine the permeability of those portions of the fault with CSPs lower than the cut-off applied in the first step). Although it allows significant flexibility, the generalized equation does not, of course, allow inclusion of all possible approaches (for example, probabilistic Shale Smear Factor; Childs *et al.* 2007; Manzocchi *et al.* 2007, or orientation-controlled slip-tendency modelling; Streit & Hillis 2005), and determining appropriate algorithms for estimating fault permeability remains an important area of active research. The modelling considerations in the current paper, however, indicate that other fault-related factors which receive less attention can also be extremely significant for managing the production uncertainty in faulted reservoirs.

APPENDIX A:

The expressions used for defining the default (Case 1) set of two-phase input fault rock properties follow Manzocchi *et al.* (2002) and are:

$$\phi_f = 0.05 k_f^{0.25}. \quad \text{(A1)}$$

$$S_{wOR} = 0.85 \quad \text{(A2)}$$

$$S_{wC} = S_{wOR} - 10^{-0.6 exp(-0.5 log_{10} k_f)} \quad \text{(A3)}$$

$$S_e = (S_w - S_{wC})/(S_{wOR} - S_{wC}) \quad \text{(A4)}$$

$$P_{CD} = 3 S_e^{-0.67} \phi_f^{0.5} k_f^{-0.5} \quad \text{(A5)}$$

$$P_{CI} = 3(1 - S_e^5) S_e^{-0.67} \phi_f^{0.5} k_f^{-0.5} \quad \text{(A6)}$$

$$k_{rw} = 0.3 S_e^3. \quad \text{(A7)}$$

$$k_{ro} = 0.85(1 - S_e)^3. \quad \text{(A8)}$$

In these equations k_f is the intrinsic (i.e. single-phase) fault rock permeability (mD), ϕ_f is fault porosity, S_w is water saturation, S_{wOR} is irreducible water saturation, S_{wC} is connate water saturation S_e is effective water saturation, P_{CI} and P_{CD} are capillary pressure for faults in the imbibition and drainage cycles (bars), and k_{rw} and k_{ro} are the water and oil relative permeabilities. The fault rock capillary threshold pressure is given from equation (A5) at an S_e value of 1.0. Note that the water saturation-dependent fault rock property curves used in the upscaling (equations A5–A8) are exclusively dependent on the intrinsic fault rock permeability (k_f).

The exponents of the capillary pressure equations were found to be among the most sensitive lamina-scale parameter on the upscaled cell pseudorelative properties in the SAIGUP models (Stephen *et al.* 2008) and, for Case 2, the exponent in the fault rock capillary pressure equations (A5, A6) is changed from 0.67 to 1.5. Petrophysically, this modification represents a reduction in grain sorting (e.g. McDougall & Sorbie 1992). In Case 3, the capillary pressure exponent is kept at 0.67, but the oil relative permeability endpoint value is made a function of absolute permeability. This follows from the observation (e.g. Al-Busafi 2005; Q. J. Fisher pers. comm. 2006) that the very limited available experimental data for low-permeability fault rock may indicate a dependence. The expression used here is $k_{ro}=k_{roEndpoint}(1-S_e)^3$, where the endpoint relative permeability is defined by the rather arbitrary expression:

$$k_{roEndpoint} = 0.85(0.25 log_{10}(k_f + 1))^{0.2 exp(-0.25 log_{10}(k_f + 1))} \quad \text{(A9)}$$

The methodological developments described have been supported by Shell, Statoil, Petrobras and recently also Total under the authors' TransGen development projects (run in conjunction with Badley Geoscience) and by the Enterprise Ireland Research Innovation fund (Contract IF/2001/354). Many of the solutions were prototyped in the EU-funded SAIGUP project (Contract ENK6-CT-2000-00073), and the datum models used were created in conjunction with SAIGUP project partners. Schlumberger provided use of their Eclipse simulator. The authors thank Graham Yielding and Karl Stephen for useful discussion, John Cole for editing the paper and Richard Jolly and Alastair Welbon for helpful reviews. We are grateful to Badley Geoscience, BG International, Roxar and Shell for their support of the SAIGUP project and for their sponsorship of the production of this thematic set.

REFERENCES

Al-Busafi, B. 2005. *Incorporation of fault rock properties into production simulation models.* PhD thesis. University of Leeds.

Al-Busafi, B., Fisher, Q.J. & Harris, S.D. 2005. The importance of incorporating the multi-phase flow properties of fault rocks into production simulation models. *Marine and Petroleum Geology,* **22**, 365–374.

Antonellini, M. & Aydin, A. 1994. Effect of faulting on fluid flow in porous sandstone reservoirs: petrophysical properties. *American Association of Petroleum Geologists Bulletin,* **78**, 355–377.

Badley Geoscience 2004. TwoPhaseGen technical description. *TransGen 3. 2 user documentation.* Badley Geoscience, Lincolnshire.

Bailey, W.R., Shannon, P.M., Walsh, J.J. & Unnithan, V. 2003. The spatial distributions of faults and deep sea carbonate mounds in the Porcupine Basin, offshore Ireland. *Marine and Petroleum Geology,* **20**, 509–522.

Beach, A., Welbon, A.I., Brockbank, P.J. & McCallum, J.E. 1999. Reservoir damage around faults: outcrop examples from the Suez Gulf. *Petroleum Geoscience,* **5**, 109–116.

Berg, S.S. & Øian, E. 2007. Hierarchical approach for simulating fluid flow in normal fault zones. *Petroleum Geoscience,* **13**, 25–35.

Bonson, C.G., Childs, C., Walsh, J.J., Schöpfer, M.P.J. & Carboni, V. 2007. Geometric and kinematic controls on the internal structure of a large normal fault in massive limestones: the Maghlaq Fault, Malta. *Journal of Structural Geology,* **29**, 336–354.

Caine, J.S., Evans, J.P. & Forster, C.B. 1996. Fault zone architecture and permeability structure. *Geology,* **24**, 1025–1028.

Childs, C., Walsh, J.J. & Watterson, J. 1990. A method for estimation of the density of fault displacements below the limits of seismic resolution in reservoir formations. *In:* Buller, A.T., Berg, E., Hjelmeland, O., Kleppe, J., Torsaeter, O. & Aasen, J.O. (eds) *North Sea Oil and Gas Reservoirs II.* Graham & Trotman, London, 193–203.

Childs, C., Watterson, J. & Walsh, J.J. 1995. Fault overlap zones within developing normal fault systems. *Journal of the Geological Society, London,* **152**, 535–549.

Childs, C., Walsh, J.J. & Watterson, J. 1996. A model for the structure and development of fault zones. *Journal of the Geological Society, London,* **153**, 337–340.

Childs, C., Walsh, J.J. & Watterson, J. 1997. Complexity in fault zone structure and implications for fault seal prediction. *In:* Møller-Pedersen, P. & Koestler, A.G. (eds) *Hydrocarbon seals – Importance for exploration and production.* Norwegian Petroleum Society (NPF), Special Publications, **7**, 61–72.

Childs, C., Manzocchi, T., Nell, P.A.R., Walsh, J.J., Strand, J.A., Heath, A.E. & Lygren, T.H. 2002. Geological implications of a large pressure difference across a small fault in the Viking Graben. *In:* Koestler, A.G. & Hunsdale,

R. (eds) *Hydrocarbon Seal Quantification*. Norwegian Petroleum Society (NPF), Special Publications, **11**, 127–139.

Childs, C., Walsh, J.J., Manzocchi, T. *et al.* 2007. Definition of a fault permeability predictor from outcrop studies of a faulted turbidite sequence, Taranaki, New Zealand. *In:* Jolley, S.J., Barr, D., Walsh, J.J. & Knipe, R.J. (eds) *Structurally Complex Reservoirs*. Geological Society, London, Special Publications, **292**, 235–258.

Crawford, B. R., Myers, R. D., Woronow, A., Faulkner, D. R. & Rutter, E. H. 2002. Porosity–permeability relationships in clay-bearing fault gouge. Paper 78214 presented at the Society of Petroleum Engineers/International Society of Rock Mechanics Conference, Iving Texas.

Dale, M., Ekrann, S., Mykkeltveit, J. & Virnovsky, G. 1997. Effective relative permeabilities and capillary pressures for one-dimensional heterogeneous media. *Transport in Porous Media,* **26**, 229–260.

Dawers, N.H. & Anders, M.H. 1995. Displacement-length scaling and fault linkage. *Journal of Structural Geology,* **17**, 607–614.

Fisher, Q.J. & Knipe, R.J. 1998. Fault sealing processes in siliciclastic sediments. *In:* Jones, G., Fisher, Q.J. & Knipe, R.J. (eds) *Faulting, Fault Sealing and Fluid Flow in Hydrocarbon Reservoirs*. Geological Society, London, Special Publications, **147**, 117–134.

Fisher, Q.J. & Knipe, R.J. 2001. The permeability of faults within siliciclastic petroleum reservoirs of the North Sea and Norwegian Continental Shelf. *Marine and Petroleum Geology,* **18**, 1063–1081.

Fisher, Q.J., Harris, S.D., McAllister, E., Knipe, R.J. & Bolton, A.J. 2001. Hydrocarbon flow across sealing faults: theoretical constraints. *Marine and Petroleum Geology,* **18**, 251–257.

Flodin, E. A., Aydin, A., Durlofsky, L. A. & Yeten, B. 2001. Representation of fault zone permeability in reservoir flow models. Paper SPE 71617, presented at the SPE Technical Conference and Exhibition, New Orleans, 30 September – 3 October.

Foxford, K.A., Walsh, J.J., Watterson, J., Garden, I.R., Guscott, S.C. & Burley, S.D. 1998. Structure and content of the Moab Fault zone, Utah, USA. *In:* Jones, G., Fisher, Q.J. & Knipe, R.J. (eds) *Faulting, Fault Sealing and Fluid Flow in Hydrocarbon Reservoirs*. Geological Society, London, Special Publications, **147**, 87–103.

Fulljames, J.R., Zijerveld, L.J.J. & Franssen, R.C.M.W. 1997. Fault seal processes: systematic analysis of fault seals over geological and production time scales. *In:* Møller-Pedersen, P. & Koestler, A.G. (eds) *Hydrocarbon seals – Importance for exploration and production*. Norwegian Petroleum Society (NPF), Special Publications, **7**, 51–59.

Gauthier, B.D.M. & Lake, S.D. 1993. Probabilistic modeling of faults below the limit of seismic resolution in Pelican Field, North Sea, offshore United Kingdom. *American Association of Petroleum Geologists Bulletin,* **77**, 761–777.

Gibson, R.G. 1998. Physical character and fluid flow properties of sandstone-derived fault zones. *In:* Coward, M.P., Daltaban, T.S. & Johnson, H. (eds) *Structural Geology in Reservoir Characterisation*. Geological Society, London, Special Publications, **127**, 83–98.

Heffer, K.J. & Bevin, T.G. 1990. Scaling relationships in Natural Fractures: data, theory and applications. SPE Paper 209819.

Hesthammer, J. & Fossen, H. 2000. Uncertainties associated with fault sealing analysis. *Petroleum Geoscience,* **6**, 37–47.

Hesthammer, J., Johansen, T.E.S. & Watts, L. 2000. Spatial relationships within fault damage zones in sandstone. *Marine and Petroleum Geology,* **17**, 873–893.

Hollund, K., Mostad, P., Nielsen, B.F. *et al.* 2002. Havana – a fault modelling tool. *In:* Koestler, A.G. & Hunsdale, R. (eds) *Hydrocarbon Seal Quantification*. Norwegian Petroleum Society (NPF), Special Publications, **11**, 157–171.

Howell, J.A., Skorstad, A., MacDonald, A., Fordham, A., Flint, S., Fjellvoll, B. & Manzocchi, T. 2008. Sedimentological parameterisation of shallow-marine reservoirs. *Petroleum Geoscience,* **14**, 17–34.

Huggins, P., Watterson, J., Walsh, J.J. & Childs, C. 1995. Relay zone geometry and displacement transfer between normal faults recorded in coal-mine plans. *Journal of Structural Geology,* **17**, 1741–1755.

Hull, J. 1988. Thickness–displacement relationships for deformation zones. *Journal of Structural Geology,* **10**, 431–435.

Imber, J., Tuckwell, G.W., Childs, C. *et al.* 2004. Three-dimensional distinct element modelling of relay growth and breaching along normal faults. *Journal of Structural Geology,* **26**, 1897–1911.

Jolley, S.J., Dijk, H., Lamens, J.H., Fisher, Q.J., Manzocchi, T., Eikmans & Huang, Y. 2007. Faulting and fault sealing in production simulation models: Brent Province, northern North Sea. *Petroleum Geoscience,* **13**, 321–340.

Knai, T.A. & Knipe, R.J. 1998. The impact of faults on fluid flow in the Heidrun Field. *In:* Jones, G., Fisher, Q.J. & Knipe, R.J. (eds) *Faulting, Fault Sealing and Fluid Flow in Hydrocarbon Reservoirs*. Geological Society, London, Special Publications, **147**, 269–282.

Lindsay, N.C., Murphy, F.C., Walsh, J.J. & Watterson, J. 1993. Outcrop studies of shale smears on fault surfaces. *In:* Flint, S.T. & Bryant, A.D. (eds) *The geological modelling of hydrocarbon reservoirs and outcrop analogues*. Special Publication of the International Association of Sedimentologists, **15**, 113–123.

Mandl, G. 1987. Discontinuous fault zones. *Journal of Structural Geology,* **9**, 105–110.

Manighetti, I., King, G., Gaudemer, Y., Sholtz, C. & Doubre, C. 2001. Slip accumulation and lateral propagation of active normal faults in Afar. *Journal of Geophysical Research,* **106**, 13667–13696.

Manzocchi, T. 1997. *Quantification of flow impairment in faulted sandstone reservoirs*. PhD thesis. Heriot-Watt University, Edinburgh.

Manzocchi, T., Ringrose, P.S. & Underhill, J.R. 1998. Flow through fault systems in high porosity sandstones. *In:* Coward, M.P., Johnson, H. & Daltaban, T.S. (eds) *Structural Geology in Reservoir Characterization*. Geological Society, London, Special Publications, **127**, 65–82.

Manzocchi, T., Walsh, J.J., Nell, P.A.R. & Yielding, G. 1999. Fault transmissibility multipliers for flow simulation models. *Petroleum Geoscience,* **5**, 53–63.

Manzocchi, T., Heath, A.E., Walsh, J.J. & Childs, C. 2002. The representation of two phase fault-rock properties in flow simulation models. *Petroleum Geoscience,* **8**, 119–132.

Manzocchi, T., Walsh, J.J., Tomasso, M., Strand, J., Childs, C. & Haughton, P. 2007. Static and dynamic connectivity in bed-scale models of faulted and unfaulted turbidites. *In:* Jolley, S.J., Barr, D., Walsh, J.J. & Knipe, R.J. (eds) *Structurally Complex Reservoirs*. Geological Society, London, Special Publications, **292**, 309–336.

Manzocchi, T., Carter, J.N., Skorstad, A. *et al.* 2008*a*. Sensitivity of the impact of geological uncertainty on production from faulted and unfaulted shallow-marine oil reservoirs – objectives and methods. *Petroleum Geoscience,* **14**, 3–15.

Manzocchi, T., Matthews, J.D., Strand, J.A. *et al.* 2008*b*. A study on the structural controls on oil recovery from shallow marine reservoirs. *Petroleum Geoscience,* **14**, 55–70.

Marle, M.G. 1981. *Multiphase flow in porous media*. Gulf Publishing Company, Houston, Texas.

Matthews, J.D., Carter, J.N., Stephen, K.D., Zimmerman, R.W., Skorstad, A., Manzocchi, T. & Howell, J.A. 2008. Assessing the effects of geological uncertainty on recovery estimates in shallow-marine reservoirs – the application of reservoir engineering to the SAIGUP project. *Petroleum Geoscience,* **14**, 35–44.

McDougall, S. R. & Sorbie, K. S. 1992. Network simulation of flow processes in strongly wetting and mixed wet porous media. Paper presented at the 3rd SPE/EAPG Conference on the Mathematics of Oil recovery, 17–19 June, Delft, The Netherlands.

Muraoka, H. & Kamata, H. 1983. Displacement distributions along minor fault traces. *Journal of Structural Geology,* **5**, 483–495.

Myers, R.D., Allgood, A., Hjellbakk, A., Vrolijk, P. & Briedis, N. 2007. Testing fault transmissibility predictions in a structurally dominated reservoir: Ringhorne Field, Norway. *In:* Jolley, S.J., Barr, D., Walsh, J.J. & Knipe, R.J. (eds) *Structurally Complex Reservoirs*. Geological Society, London, Special Publications, **292**, 271–294.

Odling, N.E., Harris, S.D. & Knipe, R.J. 2004. Permeability scaling properties of fault damage zones in siliclastic rocks. *Journal of Structural Geology,* **26**, 1727–1747.

Ottensen Ellevset, S., Knipe, R.J., Olsen, T.S., Fisher, Q.T. & Jones, G. 1998. Fault controlled communication in the Sleipner Vest Field, Norwegian continental shelf: detailed quantitative input for reservoir simulation and well planning. *In:* Jones, G., Fisher, Q.J. & Knipe, R.J. (eds) *Faulting, Fault Sealing and Fluid Flow in Hydrocarbon Reservoirs*. Geological Society, London, Special Publications, **147**, 283–297.

Ringrose, P.S. & Corbett, P.W.M. 1994. Controls on two-phase fluid flow in heterogeneous sandstones. *In:* Parnell, J. (ed.) *Geofluids: Origin, Migration and Evolution of Fluids in Sedimentary Basins*. Geological Society, London, Special Publications, **78**, 141–150.

Ringrose, P.S., Sorbie, K.S., Corbett, P.W.M. & Jensen, J.L. 1993. Immiscible flow behaviour in laminated and cross-bedded sandstones. *Journal of Petroleum Science and Engineering,* **9**, 103–124.

Rivenæs, J.C. & Dart, C.J. 2002. Reservoir compartmentalisation by water-saturated fluids – is evaluation possible with today's tools? *In:* Koestler, A.G. & Hunsdale, R. (eds) *Hydrocarbon Seal Quantification*. Norwegian Petroleum Society (NPF), Special Publications, **11**, 173–186.

Rotevatn, A., Fossen, H., Hesthammer, J., Aas, T.E. & Howell, J.A. 2007. Are relay ramps conduits for fluid flow? Structural analysis of a relay ramp in Arches National Park, Utah. *In:* Lonergan, L., Jolly, R.J.H., Rawnsley, K. & Sanderson, D.J. (eds) *Fractured Reservoirs*. Geological Society, London, Special Publications, **270**, 55–71.

Schlumberger 2005. Transmissibility calculations. *Eclipse Technical Description 2005a*. Schlumberger.

Schöpfer, M.P.J., Childs, C., Walsh, J.J., Manzocchi, T. & Koyi, H.A. 2007. Geometrical analysis of the refraction and segmentation of normal faults in periodically layered sequences. *Journal of Structural Geology,* **29**, 318–335.

Shipton, Z.K. & Cowie, P.A. 2001. Damage zone and slip-surface evolution over μm to km scales in high-porosity Navajo sandstone, Utah. *Journal of Structural Geology,* **23**, 1825–1844.

Shipton, Z.K. & Cowie, P.A. 2003. A conceptual model for the origin of fault damage zone structures in high-porosity sandstone. *Journal of Structural Geology,* **25**, 333–344.

Soliva, R. & Benedicto, A. 2004. A linkage criterion for segmented normal faults. *Journal of Structural Geology,* **26**, 2251–2267.

Sperrevik, S., Gillespie, P.A., Fisher, Q.J., Halvorsen, T. & Knipe, R. 2002. Empirical estimation of fault rock properties. *In:* Koestler, A.G. & Hunsdale, R. (eds) *Hydrocarbon Seal Quantification.* Norwegian Petroleum Society (NPF), Special Publications, **11**, 109–126.

Stephen, K.D., Yang, C., Carter, J.N., Howell, J.A., Manzocchi, T. & Skorstad, A. 2008. Upscaling uncertainty analysis in a shallow marine environment. *Petroleum Geoscience,* **14**, 71–84.

Sternlof, K.R., Chapin, J.R., Pollard, D.D. & Durlofsky, L.J. 2004. Permeability effects of deformation band arrays in sandstone. *American Association of Petroleum Geologists Bulletin,* **88**, 1315–1329.

Streit, J.E. & Hillis, R.R. 2005. Estimating fault stability and sustainable fluid pressures for underground storage of CO_2 in porous rock. *Energy,* **29**, 1445–1456.

Syversveen, A. R., Skorstad, A., Soleng, H. H., Røe, P. & Tveranger, J. 2006. Facies modelling in Fault zones. Paper presented at the 10th European conference on the mathematics of oil recovery, 4–7 September, Amsterdam, The Netherlands.

Walsh, J.J., Watterson, J., Heath, A.E., Gillespie, P.A. & Childs, C. 1998. Assessment of the effects of sub-seismic faults in bulk permeabilities of reservoir sequences. *In:* Coward, M.P., Johnson, H. & Daltaban, T.S. (eds) *Structural Geology in Reservoir Characterization.* Geological Society, London, Special Publications, **127**, 99–114.

Walsh, J.J., Bailey, W.R., Childs, C., Nicol, A. & Bonson, C.G. 2003*a*. Formation of segmented normal faults: a 3-D perspective. *Journal of Structural Geology,* **25**, 1251–1262.

Walsh, J.J., Childs, C., Imber, J., Manzocchi, T., Watterson, J. & Nell, P.A.R. 2003*b*. Strain localisation and population changes during fault system growth within the Inner Moray Firth, Northern North Sea. *Journal of Structural Geology,* **25**, 1897–1911.

Watterson, J., Walsh, J.J., Gillespie, P.A. & Easton, S. 1996. Scaling systematics of fault sizes on a large-scale range fault map. *Journal of Structural Geology,* **18**, 199–214.

Westaway, R. 1994. Quantitative analysis of populations of small faults. *Journal of Structural Geology,* **16**, 1259–1273.

Yielding, G., Needham, T. & Jones, H. 1996. Sampling of fault populations using sub-surface data: a review. *Journal of Structural Geology,* **18**, 135–146.

Yielding, G., Freeman, B. & Needham, D.T. 1997. Quantitative fault seal prediction. *American Association of Petroleum Geologists Bulletin,* **81**, 897–917.

Yielding, G. 2002. Shale Gouge Ratio: calibration by geohistory. *In:* Koestler, A.G. & Hunsdale, R. (eds) *Hydrocarbon Seal Quantification.* Norwegian Petroleum Society (NPF), Special Publications, **11**, 1–15.

Received 29 January 2007; revised typescript accepted 2 July 2007.